3D Reconstructions of Mouse Skeletal Muscle Reveal a Decrease in the MICOS Complex and Altered Mitochondrial Networks

Zer Vue[1*], Edgar Garza-Lopez[2*], Kit Neikirk[1*], Larry Vang[1], Heather Beasley[1], Andrea G. Marshall[1], Amber Crabtree[1], Antentor Hinton, Jr[1#]

[1] Department of Molecular Physiology and Biophysics, Vanderbilt University, Nashville, TN, 37232, USA.
[2] Department of Internal Medicine, University of Iowa, Iowa City, IA, 52242, USA.

*These authors share co-first authorship.
#These authors share senior authorship.

Corresponding Author:
Antentor Hinton
Department of Molecular Physiology and Biophysics
Vanderbilt University
antentor.o.hinton.jr@Vanderbilt.Edu 319-383-3095

Graphical Abstract:

ABSTRACT

Background: Skeletal muscle gradually loses mass, strength, endurance, and oxidative capacity during aging. Studies of bioenergetics and protein turnover show that mitochondria mediate this decline in function. Mitochondria are essential for the production of ATP, which occurs in the cristae, the folds of the inner mitochondrial membrane. While mitochondrial aging is associated with endoplasmic reticulum stress, fragmented mitochondria, and decreased mitochondrial capacity, the genes associated with morphological changes in mitochondria during aging are unknown. Further, we do not understand how 3D mitochondrial networks and the specialization of mitochondria alter during aging.

Methods: We measure changes in mitochondrial morphology and mitochondrial connectivity during the aging of the mouse gastrocnemius muscle through serial block facing-scanning electron microscopy and 3D reconstruction. Nanotunnels are also measured through 3D reconstruction. CRISPR/Cas9 KD is performed to examine changes in mitochondria upon loss of MICOS complex and OPA-1. Metabolomics are used to find key metabolite pathways changed upon MICOS complex loss.

Results: We found changes in mitochondrial network configuration, nanotunneling, size, shape, number, contact sites, and cristae organizing system (MICOS) dynamics and gene expression in skeletal muscle across aging. Cardiac muscle showed similar differences but less fragmentation and wide-spread changes across 2-year aaging. We also found an association of optic atrophy 1 (OPA-1) and the MICOS complex in the gastrocnemius with mitochondrial aging, decreased oxidative capacity, and altered mitochondrial metabolism.

Conclusions: We are the first to examine mitochondria changes in skeletal muscle and cardiac muscle across aging. 3D reconstructions of nanotunnels elucidated novel patterns in skeletal muscle. Notably, we noticed differences in skeletal and cardiac muscle that suggests a differential response to mitochondrial aging in cardiac and skeletal muscle. Importantly, we found similar changes in mitochondrial morphology were observed in aging skeletal muscles and for loss of MICOS proteins in mouse skeletal muscle. Furthermore, MICOS proteins decreased with age. In tandem, this suggests a relationship between the MICOS complex and aging, which further 3D reconstruction could potentially further link to disease states.

Keywords: MICOS, aging, mitochondria, 3D morphometry; imaging; machine learning; mitochondrial disease; mitochondrion; nanotunnel; reconstruction; reticulum; serial block-face SEM; skeletal muscle.

INTRODUCTION

The loss of muscle mass associated with aging, known as sarcopenia, impacts the quality of life affecting both type I and type II fibers, but more so for type II fibers [1]. Decreased mitochondrial activity, oxidative capacity, density, and biogenesis and increased mitochondrial dysfunction implicate mitochondria in sarcopenia [2,3]. Although mitochondria are typically associated with generating cellular ATP by oxidative phosphorylation [4], they are also involved in calcium homeostasis, programmed cell death, and regulation of innate immunity and stem cells. Their structure changes dynamically as they shift from fission to fusion. Important mitochondrial functions are associated with the inner membrane folds known as cristae, which house the oxidative phosphorylation machinery [5]. Disruption of optic atrophy 1 (OPA-1), an inner membrane protein that regulates mitochondrial fusion, causes mitochondrial fragmentation and affects the dimensions, shapes, and sizes of the cristae [5]. Disruption of Drp1, a protein associated with mitochondrial fission, causes elongated mitochondria and resistance to remodeling of the cristae [6,7]. Nanotunnels or “mitochondria-on-a-string” are thin, double-membrane protrusions lacking cristae that allow mitochondria to communicate across distances. Nanotunnels may increase in mitochondrial disease [8,9] and we suspect may be associated with mitochondrial dysfunction during aging.

Mutations in genes that regulate the morphology of cristae have been associated with aging cardiomyocytes [10]. These cristae morphology genes are located at the crista junctions in the inner membrane and are a part of the mitochondrial contact site and cristae organizing system (MICOS), which are important for maintaining mitochondrial shape and distances [11]. Cristae membranes contain the electron transport chain complexes and ATP synthase for ATP synthesis via oxidative phosphorylation [12–14]. Since mitochondrial morphology affects function, altering the structure by knocking out MICOS-associated genes or the GTPase of OPA-1 could alter the metabolism and function of mitochondria during aging [12–14].

Mitochondria show specialization in types and structures associated with their roles in glycolysis and oxidative metabolism in skeletal muscle [8,15–17]. However, there is little information on the role of aging on the mitochondrial genes that affect structure. We want to better understand how aging affects the specialization of mitochondria and their function. While young mitochondria show extensive specialization, it is not known whether this is true for aged

mitochondria. The gastrocnemius is a mixed muscle with both oxidative fibers containing many mitochondria and glycolytic fibers with few mitochondria. This heterogeneity makes the gastrocnemius ideal to study changes in mitochondrial dynamics. Other studies on the effects of aging on mitochondria in human and mouse skeletal muscle have focused on mitochondrial mutations [18]. Our 3D reconstruction of aged skeletal gastrocnemius muscle is a novel approach to study the connections between mitochondria and to determine how disconnections and reduced mitochondrial communication impact oxidative phosphorylation.

To better understand the relationship between mitochondria and muscle aging, we quantitatively analyzed 3D networks of specialized mitochondria at single-organelle resolution in muscle biopsies of mice at 3 months, 1 year, and 2 years of age. We compared size, shape, quantity, complexity, and branching using 3D reconstructions of aged gastrocnemius muscle, and we measured nanotunneling in mouse muscles at these three ages. Multivariate analysis was used to identify changes in metabolites, the MICOS complex, OPA-1, nanotunneling, mitochondrial complexity, and morphological changes to better understand how mitochondrial specialization and structure change during aging.

RESULTS

Aging Results in Smaller, Shorter, Poorly Connected Mitochondria with Decreased Branching in Mouse Skeletal Muscle

The mitochondrial free radical theory of aging (MRFTA) proposes that the accumulation of reactive oxygen species (ROS) byproducts of mitochondrial respiration, such as hydroxyl radicals, causes the aging damage [19–21]. Since many mitochondrial functions depend on structure [5,22,23], it is important to examine mitochondrial structural changes over time. We hypothesized that ROS causes increased mitochondrial mitophagy and fragmentation over time with concomitant losses in mitochondrial crista integrity.

Our objective was to determine how aging alters mitochondrial networks and individual mitochondria. We imaged gastrocnemius biopsies from young (3-month-old), mature (1-year-old) and aged (2-year-old) mice by serial block-face scanning electron microscopy (SBF-SEM) with resolutions of 10 µm for the x- and y- planes and 50 µm for the z-plane, which allows visualization of the electron connectome. We found structural changes in mitochondrial shape and the intermyofibrillar (IMF) region of the gastrocnemius muscle. IMF mitochondria are located between myofibrils, arranged in pairs at the z-band of each sarcomere, with 2D elongated tubular shapes [24]. However, we do not know how aging affects mitochondrial orientation, the structure of C-band sarcomeres, or the morphological changes in incomplete fission known as nanotunnels. For each region of interest across the three age groups, we analyzed 300 slices at 50 µm intervals at the transverse intervals. Approximately 50 IMF mitochondria were segmented from each image stack (Figure 1A-C) and a 3D surface view was generated (Figure 1A’’-C’’). We analyzed mitochondria sub-network volumes from four regions of interest with a total average of 175 mitochondria for each mouse (n = 3), for a total of 500 mitochondria. Mitochondrial networks in aged mice showed largely interconnected mitochondria that were not composed of a single reticulum (Figures 1A’’’–C’’’). We found that mitochondrial network volumes decreased with mitochondrial age (Figures 1 A’’’–C’’) as did mitochondrial volume (SFigure 1C). The area and perimeter of mitochondria of samples from 2-year-old mice were significantly lower than those from 3-month-old mice; however, there was no significant change

for 1-year-old mice compared to 3-month-old mice (SFigures 1A-B). This showed that the size and length of mitochondria change with age, but we do not know whether mitochondrial shape differs significantly between mice of different ages.

To understand changes in mitochondrial shape versus age, we need to measure mitochondrial complexity. To quantify the 2D form factor as a 3D shape known as mitochondrial complexity we used previously established methods [17,25]. To begin with we examined transverse (Figure 2A-C) and longitudinal (Figure 2A'-C') mitochondria across aging in skeletal muscle. These measures showed networking and broad mitochondria. Since we observed in 3D reconstructions that mitochondrial populations are heterogeneous and diverse, we utilized mito-otyping, which is the karyotype-like arrangement of mitochondria [17], to capture the diversity of IMF mitochondria (Figure 2G). These together suggest that complexity decreases across. Furthermore, we also measured sphericity to further understand changes in complexity. There was an progressive increase in sphericity with aging, which shows that complexity has decreased (SFigure 2A).

Aging Changes Mitochondria and MERC Morphology in Cardiac Muscle

To further elucidate if the changes observed across aging are unique to skeletal muscle, we also examined mitochondria morphology in cardiac muscle across 3-month, 1 year, and 2-year-old mouse. Cardiac muscle allows if mitochondria morphological changes are exclusive to skeletal muscle, since cardiac muscle allows for the comparison to different types of cells [17]. To begin with analyzing the size and shape of mitochondria, we showcase the orthoslice of the mitochondria showing representative TEM of cardiac muscle (Figure 1D-F), the overlay of the 3D reconstruction (Figure 1D'-F'), and the isolated 3D reconstruction to allow for better viewing of the structure (Figure 1D''-F''). We found that there was a decrease in perimeter, area, and volume between the 3 month and 1-year cohorts (SFigure 1A-C). In the case of perimeter and area, there was another decrease going from 1-year to 2-year; in contrast, there was a small increase for volume (Figure 1G-J). However, in all cases this decrease was less than the decrease present in skeletal muscle. Importantly, while the volumes, 3D area, and perimeter of skeletal muscle decreased heavily across aging, especially in the 2-year sample, a similar effect was not observed for cardiac muscle (Figure 1G-J). This suggests less fragmentation has occurred.

To further characterize the changes of cardiac muscle, we looked at them from both a transverse (Figure 2D-F) and longitudinal view (Figure 2D'-F'). They showcased much more packed together, smaller formations with less network formation than the skeletal muscle. From there, we again did mito-otyping of mitochondria to better categorize the diversity of the mitochondria (Figure 2H). Furthermore, the decrease in sphericity for cardiac muscle was very small (Figure 2I), so the sphericity barely changed across aging (SFigure 2B). In contrast, there was a small increase in skeletal muscle sphericity. This suggests that complexity decreased for skeletal muscle but not cardiac muscle. In combination, the aged cardiac muscle mitochondria resembled healthy mitochondria with a lack of phenotyping or fragmenting present (Figure 2). We further found that in the heart model, in contrast to the skeletal muscle, mitochondria do not develop nanotunnels (Figure 2). This led us to better quantify and analyze the nanotunnels present in skeletal muscle.

Mitochondrial Nanotunnels Change in Size and Amount with Aging in Skeletal Muscle

To quantify nanotunnels, we performed 3D reconstruction in mice at three ages, measuring 550 mitochondria per mouse (n=3) using four different regions of interest. Although nanotunnels appear to exist primarily in mitochondrial disease states [8], we found them in all three ages of mice (Figures 3A–C). The diversity and heterogeneity in the organization, sizing, and branching of nanotunnels necessitated mito-otyping (Figure 3D). We found nanotunnels in a greater proportion of mitochondria in 1-year-old mice than in 2-year-old mice (Figure 3E). However, the number of nanotunnels in each mitochondrion was significantly less in the 2-year-old mice than the 3-month-old and 1-year-old mice (Figure 3F). The length and diameter of nanotunnels increased in the older mice compared to the 3-month-old mice (Figures 3G–H), but the increase was significantly greater in the 1-year-old mice than the 2-year-old mice (Figures 3G–J). These data show that nanotunnel structure, frequency, and length change during aging.

Since mitochondrial dynamics and cristae change with aging, we measured transcripts for *Opa-1*, the gene associated with mitochondrial fusion, and *CHCHD3* (*Mic19*), *CHCHD6* (*Mic25*), *Mitofilin* (*Mic60*), the genes for the principal MICOS complex subunits. We used reverse-transcriptase qPCR (RT-qPCR) to determine the effect of aging on transcription of these genes. All of these MICOS subunits are associated with *Opa-1*, so they were expected to correlate with the amount of *Opa-1*. Since aging causes fragmentation of mitochondria, a hallmark for loss of *Opa-1* and MICOS complex proteins, we hypothesized that aging would also show decreases in the amounts of *Opa-1* and MICOS complex proteins [13,26,27]. We found progressive loss of both *Opa-1* and MICOS complex subunits, as measured by loss of transcripts for the genes encoding the proteins (SFigures 3A–D). In 1- and 2-year-old mice, the amount of mRNA made for the MICOS complex subunit genes or the *Opa-1* gene was less than half of that made in 3-month-old mice (SFigures 3A–C). Furthermore, for all MICOS genes, there was a statistically significant decrease in the amount of mRNA over time with a higher level of significance in 2-year-old mice. These data show a correlation between mitochondrial morphology changes and decreases in expression of genes for *Opa-1* and MICOS subunits *CHCHD3*, *CHCHD6*, and *Mitofilin* during aging; however, the loss of these proteins may not cause the changes.

Changes in Cristae and Mitochondria in Myotubes and Oxygen Respiration Rate Upon Knockout of MICOS complex and *Opa-1*

The MICOS complex and OPA-1 are key players in mitochondrial biogenesis [11,13,28], but how their interactions regulate aging and mitochondrial superstructures is poorly understood. To determine the role of OPA-1 and the MICOS complex, we ablated the genes for the *Opa-1* and the MICOS complex in isolated primary skeletal muscle cells from 3-month-old mice. We isolated primary satellite cells, differentiated myoblasts to myotubes. From there, we used CRISPR/Cas9, guide RNA (Table 2), and a control plasmid to transiently knockout the genes for MICOS complex components and *Opa-1* from skeletal muscle cells. As we observed previously, in vitro deletion of OPA-1 altered mitochondrial morphology [29–31].

We measured 1250 mitochondria across 10 cells. Loss of *Opa-1* was a positive control for mitochondrial morphology changes. Although *Opa-1* expression decreases with age [3], the effect of age on the MICOS complex is unknown. Using transmission electron microscopy (TEM) images, we compared mitochondria and cristae in myotubes from wild type (WT) and knockouts of *Opa-1* and *Mitofilin* genes, which are essential for the organization of mitochondrial cristae [32,33] (Figures 4A–C). Mitochondrial average area decreased for both *Opa-1* and *Mitofilin* knockout myotubes (Figure 4D), while mitochondrial circularity (the roundness and symmetry of

mitochondria) and number increased for both *Opa-1* and *Mitofilin* knockout myotubes (Figures 4E–F). For both *Opa-1* and *Mitofilin* knockouts, the number of cristae per mitochondrion decreased, as did the cristae score and cristae surface areas compared to the WT (Figures 4G–I). Cristae score measures the uniformity and regularity of cristae compared to typical cristae, with a lower number representing abnormality and dysfunction. We also compared WT with *Opa-1*, *CHCHD3*, and *CHCHD6* knockout myotubes (Figures 4P–S). Knockout of MICOS subunit *CHCHD3* ~~(CHCHD3)~~ results in fragmented mitochondria with less *Opa-1* as the cristae lose their normal structure [34]. Similarly, *CHCHD6* is important in maintaining crista structure and its downregulation results in hollow cristae lacking an electron-dense matrix, thereby inhibiting ATP production and cell growth [33,35,36]. Mitochondrial average area decreased for *Opa-1*, *CHCHD3*, and *CHCHD6* knockout myotubes (Figure 4T), while the circularity index and the number of mitochondria, once normalized, increased (Figures 4U–V). For *Opa-1*, *CHCHD3*, and *CHCHD6* knockouts, the number of cristae per mitochondrion decreased, as did the cristae score and cristae surface area compared to the WT (Figures 4W–Y). The least significant change was for the *CHCHD3* knockout. Together, these data show quantitative and structural changes in both mitochondria and cristae upon loss of MICOS proteins.

Loss of OPA-1 induces bioenergetic stress and decreased electron transport chain function [31] and ablation of the MICOS complex alters mitochondrial capacity [37,38]. We found that loss of OPA-1 or *Mitofilin* in myotubes decreased basal oxygen consumption rate (OCR) (Figures 4J–K) and decreased ATP-linked, maximum, and reserve capacity OCR (Figures 4L–N). Although OPA-1 knockout myotubes exhibited a decrease in proton leak, *Mitofilin* knockouts showed no significant difference (Figure 5O). In *Opa-1*, *CHCHD3*, and *CHCHD6* knockouts, there was a decrease in basal, ATP-linked, maximum, and reserve capacity OCR compared to the control (Figures 4Z–AD). Although proton leak OCR decreased in *Opa-1* and *CHCHD3* knockout myotubes, there was no significant difference between the control and *CHCHD6*. The decrease in OCR may be attributed to smaller and fragmented mitochondria; mitochondrial density decreases as fragmentation targets them for autophagy [3,39]. Together, these results show that MICOS and *Opa-1* are essential for normal respiration of muscle tissue.

TEM provides mitochondrial detail, but not 3D morphology; therefore, we used SBF-SEM to look at the 3D structure of the mitochondria. Using myotubes with ablated genes for *Opa-1* and MICOS complex subunits, as described above, we measured a total of 200 mitochondria across 10 cells. We compared mitochondria in WT, *Opa-1* knockout, and *Mitofilin* knockout myotubes (Figures 5A–C) and found that compared to the elongated mitochondria in the WT, the 3D length was much shorter in *Opa-1* and *Mitofilin* knockouts (Figure 5D), and the volume of the mitochondria was less (Figure 5E). In similar experiments, we compared mitochondria in WT to those in *Opa-1*, *CHCHD3*, and *CHCHD6* knockout myotubes (Figures 5F–I) and found shorter mitochondria in the three knockout strains (Figure 5D). Similarly, the volume of mitochondria was also less in *CHCHD3*, *CHCHD6*, and *Opa-1* knockouts compared to the control (Figure 5E). The 3D reconstruction data, in combination with the prior TEM results, show how mitochondrial dynamics change with the loss of MICOS subunits.

Metabolomics Show Key Metabolite Changes in Knockout of MICOS Complex Proteins and *Opa-1* in Myotubes.

To determine the global effects of loss of *Opa-1* or the MICOS complex in skeletal muscle myotubes, we analyzed the metabolome to identify changes in metabolites that occurred with changes in mitochondria and cristae. Principal component analysis (PCA) revealed distinct

populations in the control and the *Mitofilin* knockout strains, which suggested that their genotypes contributed to the clustering (Figure 6A). To identify metabolites with the most robust ability to discriminate between true positives and false positives, we constructed a model using analysis of variance (ANOVA) to determine several key metabolites that were statistically significant (Figure 6B). This unique metabolite signature revealed that *Mitofilin* plays a critical role in regulating amino acid metabolism and steroidogenesis (Figures 6C–D). Upregulation of steroidogenesis pathways may result from the increased fluidity of membranes caused by *Mitofilin* [40,41]. We also measured the effect of ablation of genes for *CHCHD3* and *CHCHD6* in skeletal muscle myotubes on bioenergetic metabolism. PCA revealed distinct populations in the control and the *CHCHD3* and CHCHD6 knockouts, which showed a similar profile (Figure 6E). We constructed a model using ANOVA to determine which metabolite changes in *CHCHD3* and *CHCHD6* knockouts were statistically significant (Figure 6F) There was a loss of protein synthesis and changes in carbohydrate metabolism (Figures 6G–H). Loss of *Opa-1* typically favors fatty acid synthesis, so these results showing increased carbohydrate metabolism differ from previous *Opa-1* knockout responses [42–44]. This atypical response was evident in the increase in lactose and starch synthesis, but there was poor protein turnover, as seen in methionine metabolism (Figure 6H).

DISCUSSION

Mitochondrial morphology is linked to oxidative phosphorylation [4,17,22]. We produced high-resolution three-dimensional mitochondrial images and measured mitochondria in myotubes of aging skeletal muscles lacking components of the MICOS complex. We demonstrated that either aging or loss of MICOS proteins in skeletal muscle resulted in the loss of mitochondrial function, suggesting a correlation between aging and MICOS protein expression.

Previous studies using 3D focused ion beam-scanning electron microscopy (FIB-SEM) in human skeletal muscle [45] and in mouse muscle [46] characterized the networking of the mitochondria. Vincent et al. did quantitative 3D reconstructions using SBF-SEM to define the morphological differences in the skeletal muscles of humans versus mice, and they compared patients with primary mitochondrial DNA diseases with healthy controls [17]. However, our study is the first to look at the 3D morphology of mouse mitochondria in aged skeletal muscle.

We studied skeletal muscle because it is important in movement and is affected by aging. Mitochondria comprise ~6% of the cell volume in skeletal muscle [47] providing the high energy levels needed by skeletal muscle [47]. Skeletal muscle has type I slow-twitch muscle fibers or type II fast-twitch muscle fibers; type I fibers are more effective for endurance, while type II fibers better support short bursts of muscle activity [47–49]. Our studies could not distinguish the two fiber types, although we observed many variable muscle fibers within a cell and between all differently aged cohorts.

Skeletal muscle may induce mitochondrial biogenesis by activating adenosine monophosphate-activate protein kinase (AMPK) [48], which may explain the loss of skeletal muscle function in aging that results from increased apoptosis, decreased regeneration rate, and reduced mobility [19,20,49]. Using 3D reconstructions, we found that all parameters of the mitochondria changed during aging including volume, sphericity, area, and perimeter (Figure 1G-J), and the mitochondria became less interconnected, possibly as a result of decreased

mitochondrial fusion. We also saw a decrease in the MBI and MCI during aging, which shows that mitochondria lose sphericity as they age (Figure 2).

The change in morphology in aging mitochondria might be explained by the mitochondrial free radical theory of aging (MFRTA), which hypothesizes that the ROS byproducts of respiration result in hydroxyl radicals that damage every part of the body [19,20]. According to this theory, aerobic respiration and ATP production by mitochondria are ultimately responsible for aging [20,50]. The MFRTA also proposes that ROS alter other functions of mitochondria, including ATP production, as they induce aging [50]. Since oxidative stress may also be linked to diabetes [51], understanding the association between aging and mitochondria is important.

We found nanotunnels, which are thin, double-membrane mitochondrial connections that can transport proteins and nutrients, in all skeletal muscle samples. While healthy humans have almost no nanotunnels [17], we found the most nanotunnels in the skeletal muscle of 1-year-old mice, a moderate number in healthy 3-month-old mice (Figures 3E–H), and an even higher number in some 2-year-old skeletal muscle. The 2-year-old skeletal muscle would be predicted to be diseased and should, therefore, have the most nanotunnels, but we did not observe this [8,52]. The 2-year-old samples may have shown fewer nanotunnels if the high rate of fragmentation (Figure 1) and lack of connectedness (Figure 2) prevented nanotunnel formation. In contrast, the 1-year-old samples were not as fragmented, and, despite the disease-like state, the remaining networks resulted in increased nanotunnels. The nanotunnels in the 3-month-old mouse skeletal muscle suggest significant differences in mouse versus human muscle [17]. We also found another key indicator of aging, increased fat mass, which is associated with a risk for insulin resistance and diabetes [53] in the 2-year-old mouse skeletal muscle. This increased fat mass that occurred in all our aging samples is associated with an increased risk of obesity and may be correlated with fragmented mitochondria.

In contrast, different results were observed when cardiac muscle mitochondria were examined across aging. In cardiac muscle, the mitochondria underwent less fragmenting and less network formation since they did not form nanotunnels (Figure 1D-F). We also found lesser complexity in the cardiac mitochondria (Figure 2I) and generally across aging, the mitochondria underwent lesser changes than skeletal muscle (2G-H). It is possible that heart and skeletal muscle respond to aging differently due to differences in nucleation. Skeletal muscles are typically multi-nucleated. As such, even if mitochondria are fragmented, they can still function through the sharing of materials. In contrast, heart cells are mono-nucleated. As a result, it may be harder for heart to recover materials in the loss of mitochondrial efficiency. As such, more resources may be dedicated to ensuring that mitochondria maintain their form, and thus their function in cardiac muscle. This highlighted the importance of further exploring how changes in skeletal muscle specifically affect their form and function through the knockout of the MICOS complex, which we believe may be implicated in aging.

MICOS proteins play key regulatory roles in mitochondrial structure and function [13,28,39]. We determined by TEM 3D reconstructions that the loss of *Mitofilin*, *CHCHD3*, and *CHCHD6* (Figures 3−5) resulted in fragmentation, disrupted cristae, and smaller mitochondria (Figures 4A–I, Figures 4P–Y; Figure 5), similar to the loss of OPA-1, which is known to cause changes in oxidative phosphorylation (Figures 4Z–AE) [13,26,31]. Overall, mitochondria lacking the MICOS genes had characteristics similar to those of aged mouse skeletal muscle (Figures 1−2). Thus, changes in mitochondrial morphology due to aging may be caused by a lack of MICOS gene expression. This is supported by the RT-qPCR data that showed decreased *CHCHD3*, *CHCHD6*,

Mitofilin, and *Opa-1* transcription with aging (SFigure 3). Although there is a link between aging and loss of *Opa-1* [3,27], little is known about the role of the MICOS complex in aging. Changes in mitochondrial architecture and loss of integrity may be caused by decreased MICOS proteins; thus, it will be important to develop methods to restore MICOS proteins and *Opa-1* lost during aging to decrease the deleterious effects of mitochondrial free radicals. Although studies have examined the role of knockouts on mitochondrial dynamics, few studies have examined how loss of MICOS proteins may be restored to mitochondria [26,54].

Many studies have analyzed the mitochondrial metabolome using mouse skeletal muscles [47,55–59]. We found that loss of *Mitofilin* affected cristae morphology (Figures 5G–I), decreased oxidative phosphorylation (Figure 4J), and may have increased lipid and steroid synthesis, which may be important for mitochondrial endoplasmic reticulum contact (MERC) regulation and cristae formation. We found an increase in tryptophan and methyl histidine metabolism (Figure 6D) and an increase in taurine metabolism and hypotaurine, a key sulfur-containing amino acid for the metabolism of fats. Loss of *Opa-1* also changes amino acid and lipid metabolism, similar to the loss of *Mitofilin* [42–44]. Steroidogenesis, which makes the membrane less rigid, was increased. Since the loss of *Mitofilin*, *CHCHD6*, or *CHCHD3* caused a loss of oxidative capacity (Figure 4), increased steroid synthesis may allow the cell to recover bioenergetic functions, as steroid compounds decrease membrane viscosity, with the incorporation of estrogen [40]. In the absence of *Mitofilin*, the cristae junctions and contact sites fall apart [60]; thus, *Mitofilin* is critical for maintaining cristae [61,62]. Cells lacking *Mitofilin* may make steroids to help the membrane to reconfigure broken cristae. Since the loss of *Opa-1* causes more MERCs [21], loss of *Mitofilin* may increase phospholipids (Figure 6D) because of increased smooth MERCs, which are associated with lipid changes [63]. This is supported by the fact that biosynthesis of phosphatidylethanolamine and phosphatidylcholine and metabolism of arachidonic acid and sphingolipid increased with loss of *Mitofilin* (Figure 6D). Since these phospholipids aggregate around MERCs and may shuffle into the endoplasmic reticulum (ER), *Mitofilin* may be a critical gene for regulating cristae morphology and with a key role in regulating mitochondrial metabolism, which is novel.

Loss of *Mitofilin* may lead to ER stress, which, via ATF4, activates amino acid transporters [64] that activate mTORC1. This leads to inefficiency in energy use since glucose homeostasis is affected by mTORC1. ER stress activates mTORC as a result of a decrease in glucose [59], resulting in changes in autophagy, which may explain why deletion of MICOS in *Drosophila* increases autophagy [39]. Loss of *Opa-1* increases ER stress [31], and loss of *Mitofilin* may cause a similar increase in amino acid catabolism. If ER stress activates amino acid transporters, branched-chain amino acids could increase ER stress, resulting in a positive feedback loop that affects the health of the cell, cellular energy, metabolism, and antioxidants. ER stress may also be responsible for the poor performance and fragmentation of mitochondria (Figure 5). Loss of *Mitofilin* may result in the breakdown of protein pathways that regulate ER stress. Other amino acid pathways, such as homocysteine (Figure 5D), are involved in triglyceride uptake and increased intracellular cholesterol, suggesting that proteins like ATF4 [59] and the MICOS complex [11,28] are important for aging. In particular, the MICOS components may prevent mitochondrial fragmentation by blocking ER stress pathways in aging. Further studies are needed to better understand the role of MICOS in MERC formation and the relation between smooth MERC and lipid synthesis.

Although *Mitofilin* is a key component of the MICOS complex, other components are likely also important. Mic10 has a role beyond organizing cristae by also binding to ATP synthase, independent of oligomerization, to support respiration and metabolic adaptation [65]. The

loss of *CHCHD3* or *CHCHD6* leads to a decrease in and disassembly of all *Mitofilin* subcomplex components in mammals, with abnormal cristae morphology and growth defects [35,66–71]. Downregulation of *CHCHD3* is linked to type 2 diabetes [72]. In our metabolomics enrichment dataset (Figure 7H), loss of *CHCHD3* or *CHCHD6* in mouse myotubes resulted in a preference for alternative fuel sources, such as lactate, lactose, and starches. Supplementation of healthy myotubes with galactose leads to a 30% increase in oxidative capacity (i.e., OCR) due to an increase in AMPK phosphorylation and cytochrome c oxidase (COX) activity, thereby forcing cells to become more oxidative to maintain ATP levels [73]. In our samples, as oxidative metabolism decreased, anaerobic metabolism and lactate levels increased, forcing cells to produce ATP by anaerobic glycolysis. However, long and high-level exposure to D-galactose generates free radicals, which alter MERCs, cause mitochondrial dysfunction, and induce aging [20,74]. This is the likely explanation for mitochondrial fragmentation in aged samples and loss of the MICOS complex, which should be investigated further.

In conclusion, we present a quantitative evaluation of mitochondrial and cristae morphology in mouse skeletal muscle using 3D reconstructions and TEM analysis. We found oxidative differences upon loss of MICOS proteins. 3D reconstructions of nanotunnels in mitochondria showed novel patterns with a moderate number of nanotunnels in young skeletal mouse tissue and relatively low numbers in the most aged mouse skeletal muscles. This suggests that in mouse skeletal muscles, nanotunnels may be more than a disease marker. Similar changes in mitochondrial morphology were observed in aging muscles and for loss of MICOS proteins in mouse skeletal muscle, and MICOS proteins decreased with age. This suggests a relationship between the MICOS complex and aging, and further studies through 3D reconstruction could elucidate the linkage between age-related muscle dysfunction, the MICOS complex, and disease states in mitochondria.

EXPERIMENTAL PROCEDURES

Animal Care and Maintenance

All procedures for the care of mice were in accordance with humane and ethical protocols approved by the University of Iowa Animal Care and Use Committee (IACUC) following the National Institute of Health Guide for the Care and Use of Laboratory Animals as described previously [31]. All experiments used WT male C57Bl/6J mice housed at 22°C on a 12-hour light, 12-hour dark cycle with free access to water and standard chow. Mice were anesthetized with 5% isoflurane/95% oxygen.

RNA Extraction and RT-qPCR

Total RNA was extracted from tissue using TRIzol reagent (Invitrogen), purified with the RNeasy kit (Qiagen Inc), and quantitated by the absorbance at 260 nm and 280 nm using a NanoDrop 1000 (NanoDrop products, Wilmington, DE, USA) spectrophotometer. Total RNA (~1 µg) was reverse-transcribed using a High-Capacity cDNA Reverse Transcription Kit (Applied Biosciences, Carlsbad CA) followed by real-time quantitative PCR (qPCR) reactions using SYBR Green (Life Technologies, Carlsbad, CA) [76]. Triplicate samples for qPCR (~50 ng) in a 384-well plate were placed into ABI Prism 7900HT instrument (Applied Biosystems) programmed as follows: 1 cycle at 95°C for 10 min; 40 cycles of 95°C for 15 s; 59°C for 15 s, 72°C for 30 s, and 78°C for 10 s; 1 cycle of 95°C for 15 s; 1 cycle of 60°C for 15 s; and one cycle of 95°C for 15 s. Data were normalized to glyceraldehyde-3-phosphate dehydrogenase

(*GAPDH*), and results are shown as fold changes. qPCR primers were designed using Primer-Blast or were previously published sequences [31] as shown in Table 1.

Table 1: qPCR Primers Used

Gene	Primers	
Opa-1	Forward	5'-ACCAGGAGACTGTGTCAA-3'
	Reverse	5'-TCTTCAAATAAACGCAGAGGTG-3'
CHCHD3	Forward	5'-GAAAAGAATCCAGGCCCTTCCACGCGC-3'
	Reverse	5'-CAGTGCCTAGCACTTGGCACAACCAGGAA-3'
CHCHD6	Forward	5'-CTCAGCATGGACCTGGTAGGCACTGGGC-3'
	Reverse	5'-GCCTCAATTCCCACATGGAGAAAGTGGC-3'
Mitofilin	Forward	5'-CCTCCGGCAGTGTTCACCTAGTAACCCCTT-3'
	Reverse	5'-TCGCCCGTCGACCTTCAGCACTGAAAACCTAT-3'

Isolation of Satellite Cells

Satellite cell differentiation was performed as previously described with slight modifications [29,31]. Gastrocnemius muscles were dissected from 8−10 week- old WT mice and washed twice with 1× PBS supplemented with 1% penicillin-streptomycin and Fungizone (300 mL/100 mL). DMEM-F12 medium with collagenase II (2 mg/mL), 1% penicillin-streptomycin, and Fungizone (300 mL/100 mL) was added to the muscle which was agitated for 90 min at 37°C. For the second wash, collagenase II was changed to 0.5 mg/mL, and the muscle was agitated for 30 min at 37°C. The tissue was cut, passed through a 70 mm cell strainer, and after centrifugation satellite cells were plated on BD Matrigel-coated dishes. To differentiate cells into myoblasts, a mixture of DMEM-F12, 20% fetal bovine serum (FBS), 40 ng/mL basic fibroblast growth factor (bFGF, R and D Systems, 233-FB/CF), 1× non-essential amino acids, 0.14 mM β-mercaptoethanol, and 1× penicillin/streptomycin, and Fungizone was used. Myoblasts were maintained with 10 ng/mL bFGF and when cells reached 80% confluence, myoblasts were differentiated in DMEM-F12, 2% FBS, 1× insulin–transferrin–selenium medium. Cells were cultured at 37°C, 5% CO_2 Dulbecco's modified Eagle's medium (DMEM; GIBCO) supplemented with 10% FBS (Atlanta Bio selected), and 1% penicillin-streptomycin (Gibco, Waltham, MA, USA).

CRISPR-Cas9 Knockouts

After three days, myotubes were infected with adenovirus to produce the following knockouts—control CRISPR/Cas9 (sc-418922), *CHCHD6* (Mic25) CRISPR (sc-425817), *CHCHD3* (Mic19) CRISPR (sc-425804), and *mitofilin* (Mic60) CRISPR (sc-429376) (Santa Cruz Biotechnology, California, US), with the use of guide RNA (Table 2). We incubated 2.5% relevant CRISPR, 2.5% RNAiMax (ThermoFisher Scientific; 13778075), and 95% Opti-MEM (Gibco; 31985070) in a tube for 20 minutes. Cells were washed twice with PBS after removal of the medium and 800 µl of OPT-MEM and 200 µL of the CRISPR mixture were added to each well. Cells were incubated for 4 hours at 37 C, 1.0 mL of DMEM medium was added, cells were incubated overnight The myotubes were then washed with PBS and the medium was replaced. Experiments were performed between 3 and 7 days after infection for a total of 6 days of differentiation.

Table 2: Guide RNA and Plasmids Used

Gene Name	Type of Plasmid	CAS Number
Mitofilin	CRISPR/Cas9 KO (m)	sc-429376

CHCHD6	CRISPR/Cas9 KO (m)	sc-425817
CHCHD3	CRISPR/Cas9 KO (m)	sc-425804
Control	CRISPR/Cas9 KO (m)	sc-418922

Serial Block-Face Scanning Electron Microscope (SBF-SEM) Processing of Mouse Muscle Fibers

SBF-SEM was performed as described previously [30,77,78]. Male mice were anesthetized with 5% isoflurane. Once the hair and skin were removed, the hindlimbs were incubated in 2% glutaraldehyde with 100 mM phosphate buffer for 30 min. Gastrocnemius muscles were dissected, cut into 1-mm^3 cubes, and incubated in 2.5% glutaraldehyde, 1% paraformaldehyde, 120 mM sodium cacodylate solution for 1 hour. Tissues were washed three times with 100 mM cacodylate buffer at room temperature before immersion in 3% potassium ferrocyanide and 2% osmium tetroxide for 1 hour at 4°C, then treated with 0.1% thiocarbohydrazide, 2% filtered osmium tetroxide for 30 min, and left overnight in 1% uranyl acetate at 4°C. Between each step, three de-ionized water washes were performed. The following day, samples were immersed in 0.6% lead aspartate solution for 30 min at 60°C and dehydrated in graded concentrations of acetone. Dehydration was for five min each in 20%, 50%, 70%, 90%, 95%, and 100% acetone.. Tissues were impregnated in Epoxy Taab 812 hard resin, then embedded in fresh resin, and polymerized at 60°C for 36–48 hours. Once polymerization was complete, blocks were sectioned for TEM to identify areas of interest, trimmed to 0.5 mm × 0.5 mm, and glued to aluminum pins. Afterward, pins were placed in an FEI/Thermo Scientific Volumescope 2 SEM, a state-of-the-art SBF imaging system. We obtained 300−400 ultrathin (0.09 µm) serial sections from the blocks that were processed for conventional TEM. All sections were collected onto formvar-coated slot grids (Pella, Redding CA), stained, and imaged as previously described [30,77,78].

Quantification of TEM Micrographs and Parameters Using ImageJ

Quantification of TEM images was performed as described previously using the National Institutes of Health (NIH) *ImageJ* software [29,30]. Cells were divided into four quadrants and two quadrants were selected randomly for complete analysis. From each individual, a minimum of 10 cells were measured with three analyses to obtain accurate and reproducible values. If variability occurred, the number of cells was expanded to 30 cells per individual to reduce the variability.

Segmentation and Quantification of 3D SBF-SEM Images Using Amira

For 3D reconstruction, SBF-SEM images were manually segmented in Amira as described previously [30,77]. All serial sections (300−400 slices) were loaded onto Amira and structural features were traced manually on sequential slices of micrograph blocks. Structures in mice were collected from 30–50 serial sections that were then stacked, aligned, and visualized using Amira to make videos and quantify volumetric structures. An average of 500 total mitochondria across four regions of interest from 3 mice were collected for quantification. For 3D reconstruction of myotubes, approximately 20 mitochondria from a minimum of 10 cells were collected. Quantification of SBF-SEM images was performed as described previously [77] using the Amira software (Thermo Scientific). Many parameters were automatically measured by Amira. For useful metrics that are not automated, algorithms for those measurements were entered manually.

Data Analysis

All SBF-SEM and TEM data were presented as the mean of at least three independent experiments with similar outcomes. Results were presented as mean ± standard error with individual data points shown. Data with only two groups were analyzed using an unpaired, t-test. For nanotunnel quantification, a Mann-Whitney test (unpaired, nonparametric) t-test was performed between two groups. If more than two groups were compared, one-way ANOVA was performed, and significance was assessed using Fisher's protected least significant difference (LSD) test. GraphPad Prism software package was used for t-tests and ANOVA analyses (La Jolla, CA, USA). For all statistical analyses, $p < 0.05$ indicated a significant difference. Higher degrees of statistical significance (**, ***, ****) were defined as $p < 0.01$, $p < 0.001$, and $p < 0.0001$, respectively.

Gas Chromatography-Mass Spectrometry (GC-MS)

Samples were extracted for metabolites in −80°C 2:2:1 methanol/acetonitrile/water that contained a mixture of nine internal standards (d_4-citric acid, $^{13}C_5$-glutamine, $^{13}C_5$-glutamic acid, $^{13}C_6$-lysine, $^{13}C_5$-methionine, $^{13}C_3$-serine, d_4-succinic acid, $^{13}C_{11}$-tryptophan, d_8-valine; Cambridge Isotope Laboratories) at a concentration of 1 µg/mL each, at a ratio of 18:1 (extraction solvent:sample volume). Cells were lyophilized overnight before extraction and homogenized with a ceramic bead mill homogenizer after the addition of extraction buffer. Samples were incubated for one hour at −20°C and centrifuged at maximum speed for 10 min. All supernatants were transferred to fresh tubes and pooled quality control (QC) samples were prepared by adding an equal volume of each sample to a fresh 1.5 mL microcentrifuge tube. A speed vac was used to evaporate the pooled QCs, samples, and processing blanks, which were made by adding extraction solvent to microcentrifuge tubes. Derivatives of the dried products were obtained using methoxamine hydrochloride (MOX) and *N*,O-bis(trimethylsilyl)trifluoroacetamide (TMS). Products were rehydrated in 30 µL of 11.4 mg/mL Molybdenum Carbide (MOC) in anhydrous pyridine (VWR), vortexed for 10 minutes, and incubated at 60°C for 1 hour. Then 20 µL of TMS was added, vortexing was repeated for one min, and samples were heated for an hour at 60°C. Samples of 1 µL were analyzed by GC-MS using a Thermo Trace 1300 GC with a TraceGold TG-5SilMS column for GC chromatographic separation. The GC temperature was set at 250°C for the inlet, with the oven temperature at a gradient with 3 min at 80 °C, increasing by 20°C a minute to a final 280°C for the last 8 minutes. The settings for the GC machine were 20:1 split ratio, split flow; 24 µL/min, purge flow; 5 mL/min, carrier mode; constant flow, carrier flow rate: 1.2 mL/min. Between each injection sample, the column was washed three times with pyridine. Metabolites were detected using the Thermo ISQ single quadrupole mass spectrometer, with data acquired from 3.90 to 21.00 min in the EI mode (70 eV) by single-ion monitoring. The profiling of the metabolites was performed using TraceFinder 4.1 with standard verified peaks and retention times. TraceFinder was used to compare metabolite peaks in each sample against an in-house library of standards. For these standards, retention times and fragment ions for each were analyzed, with fragment ions for both the target peak and two confirming ions. For the samples, we identified metabolites that matched both retention times and the three fragment ions. TraceFinder was also used for GC-MS peak integration to obtain peak areas for each metabolite. After this analysis, we used previously described protocols [79] to correct for drift over time by using QC samples run at both the beginning and end of the sequence. The data was then normalized to an internal standard to control for extraction, derivatization, and/or loading effects.

Liquid Chromatography-Mass Spectrometry (LC-MS)
Myotubes were dried, rehydrated in 40 µL acetonitrile:water (1:1), and vortexed. For LC-MS, 2 µL of the sample was used with a Thermo Q Exactive hybrid quadrupole Orbitrap mass spectrometer with a Vanquish Flex UHPLC system and a Millipore SeQuant ZIC-pHILIC column (length area = 2.1 × 150 mm, 5 µm particle size) with a ZIC-pHILIC guard column (length area = 20 × 2.1 mm). The mobile phase comprised solvent A (20 mM ammonium carbonate [$(NH_4)_2CO_3$] and 0.1% ammonium hydroxide [NH_4OH]) and solvent B (acetonitrile). The mobile phase gradient started at 80% solvent B, decreased to 20% solvent B over 20 min, returned to 80% solvent B in 0.5 min, and was held at 80% for 7 min [80]. From there, the mass spectrometer was operated in the full-scan, polarity-switching mode for 1 to 20 min, spray voltage set to 3.0 kV, capillary heated at 275°C, and HESI probe heated at 350°C. The sheath gas flow, auxiliary gas flow, and sweep gas flow were 40 units, 15 units, and 1 unit, respectively. We examined an *m*/*z* range of 70–1000, the resolution was set at 70,000, the AGC target at 1×10^6, and the maximum injection time was set to 200 ms [79].
TraceFinder 4.1 software was used for analysis and metabolites were identified based on an in-house library. Drift was corrected for as described above [79]. Data were normalized and further visualization and analysis were performed on MetaboAnalyst 5.0 [81].

Analyzing Metabolomic Data
Metabolomic analysis was performed as described previously [82] on a web service called MetaboAnalyst 5.0 (https://www.metaboanalyst.ca/MetaboAnalyst/ModuleView.xhtml, last accessed on 8 February 2022) that combines machine learning methods and statistics to group data using PCA, heat mapping, metabolite set enrichment analysis, and statistical analysis. One-way ANOVA and Fisher's LSD multiple comparison test were also used. PCA uses score plots to provide an overview of variance for the principal components. Heatmaps separate hierarchical clusters leading to progressively larger clusters. Clusters are based on similarity using Euclidean distance and Ward's linkage to minimize the clustering needed. Metabolite Set Enrichment Analysis (MSEA), which determines whether a set of functionally related metabolites is altered, can be used to identify consistent changes across many metabolites with similar roles. Overrepresentation analysis determines whether a group of compounds is overrepresented in comparison to pure chance and whether a group of metabolites have similar changes. In this analysis, the fold enrichment was calculated by dividing the observed hits by the expected metabolites. Expected number of hits are calculated by MetaboAnalyst 5.0. GraphPad Prism software (La Jolla, CA, USA) was used for statistical analysis with data expressed as mean ± standard deviation, and one-tailed p-values ≤ 0.01 were considered significant.

Measurement of OCR Using Seahorse
To measure cellular respiration, the XF24 extracellular flux (XF) bioanalyzer (Agilent Technologies/Seahorse Bioscience, North Billerica, MA, USA) was used. Cells were plated at a density of 2×10^4 per well and differentiated. After 3 days of differentiation, *Opa-1*, *CHCHD3*, *CHCHD6*, or *Mitofilin* genes were knocked down as described above. Three days after knockout, the medium was changed to XF-DMEM, and cells were kept in a non-CO_2 incubator for 60 min. The basal OCR was measured in XF-DMEM. Oxygen consumption was also measured after the addition of oligomycin (1 µg/mL), carbonyl cyanide 4-(trifluoromethoxy)phenylhydrazone (FCCP; 1 µM), rotenone (1 µM), or antimycin A (10 µM) [83]. Cells were then switched to glucose-free XF-DMEM and kept in a non-CO_2 incubator for 60 min for the glycolysis stress

test. Seahorse experimental data are for triplicate Seahorse plates. Three independent experiments were performed with four to six replicates for each time and for each condition and representative data from the replicates are shown.

NOVELTY AND SIGNIFICANCE

It is known that aging causes fragmentation and alters mitochondria dysfunction. However, we have further expanded upon these results in sever ways. We have examined the specific structural changes across aging in mitochondria. We are also the first to examined changes in nanotunnel structure, specifically using 3D reconstruction, across aging. We have found an MICOS complex implication for protection of mitochondria morphology protection against aging. We are novel for using SBF-SEM volume scope and 3D reconstruction to describe fine details in mitochondria morphology across both aging and loss of MICOS complex. We are furthermore the first to examine nanotunnels in skeletal muscle and cardiac muscle and use 3D reconstruction. Importantly, we are the first to examine mitochondrial changes across aging in mouse skeletal muscle and cardiac muscle, which we furthermore were able to compare.

ACKNOWLEDGEMENTS

We would like to thank Melanie McReynolds for her advice on processing metabolomic samples and Mariya Sweetwyne for her advice as an aging expert.

FUNDING

This work was supported by UNCF/BMS EE United Negro College Fund/Bristol-Myers Squibb E.E. T-32, number DK007563 entitled Multidisciplinary Training in Molecular Endocrinology to Z.V.; Just Postgraduate Fellowship in the Life Sciences Fellowship to H.K.B.; NSF MCB #2011577I to S.A.M.; The United Negro College Fund/Bristol-Myers Squibb E.E. Just Faculty Fund, Burroughs Wellcome Fund Career Awards at the Scientific Interface Award, Burroughs Wellcome Fund Ad-hoc Award, National Institutes of Health Small Research Pilot Subaward to 5R25HL106365-12 from the National Institutes of Health PRIDE Program, DK020593, Vanderbilt Diabetes and Research Training Center for DRTC Alzheimer's Disease Pilot & Feasibility Program to A.H.J. Its contents are solely the responsibility of the authors and do not necessarily represent the official view of the NIH. The funders had no role in study design, data collection and analysis, decision to publish, or preparation of the manuscript.

CONFLICT OF INTEREST

The authors declare that they have no conflict of interest.

REFERENCES

1. Miljkovic N, Lim J-Y, Miljkovic I, Frontera WR. Aging of skeletal muscle fibers. *Annals of rehabilitation medicine*. 2015;39:155.

2. Figueiredo PA, Mota MP, Appell HJ, Duarte JA. The role of mitochondria in aging of skeletal muscle. *Biogerontology*. 2008;9:67–84.

3. Tezze C, Romanello V, Desbats MA, Fadini GP, Albiero M, Favaro G, Ciciliot S, Soriano ME, Morbidoni V, Cerqua C, Loefler S, Kern H, Franceschi C, Salvioli S, Conte M, Blaauw B, Zampieri S, Salviati L, Scorrano L, Sandri M. Age-Associated Loss of OPA1 in Muscle

Impacts Muscle Mass, Metabolic Homeostasis, Systemic Inflammation, and Epithelial Senescence. *Cell Metab*. 2017;25:1374-1389.e6.

4. Friederich M, Hansell P, Palm F. Diabetes, oxidative stress, nitric oxide and mitochondria function. *Current diabetes reviews*. 2009;5:120–144.

5. Cogliati S, Enriquez JA, Scorrano L. Mitochondrial cristae: where beauty meets functionality. *Trends in biochemical sciences*. 2016;41:261–273.

6. Otera H, Ishihara N, Mihara K. New insights into the function and regulation of mitochondrial fission. *Biochimica et Biophysica Acta (BBA)-Molecular Cell Research*. 2013;1833:1256–1268.

7. Favaro G, Romanello V, Varanita T, Desbats MA, Morbidoni V, Tezze C, Albiero M, Canato M, Gherardi G, De Stefani D. DRP1-mediated mitochondrial shape controls calcium homeostasis and muscle mass. *Nature communications*. 2019;10:1–17.

8. Vincent AE, Turnbull DM, Eisner V, Hajnóczky G, Picard M. Mitochondrial Nanotunnels. *Trends Cell Biol*. 2017;27:787–799.

9. Zhang L, Trushin S, Christensen TA, Bachmeier BV, Gateno B, Schroeder A, Yao J, Itoh K, Sesaki H, Poon WW. Altered brain energetics induces mitochondrial fission arrest in Alzheimer's Disease. *Scientific reports*. 2016;6:1–12.

10. Zhang J, He Z, Fedorova J, Logan C, Bates L, Davitt K, Le V, Murphy J, Li M, Wang M, Lakatta EG, Ren D, Li J. Alterations in mitochondrial dynamics with age-related Sirtuin1/Sirtuin3 deficiency impair cardiomyocyte contractility. *Aging Cell*. 2021;20:e13419.

11. Kozjak-Pavlovic V. The MICOS complex of human mitochondria. *Cell and tissue research*. 2017;367:83–93.

12. Rampelt H, Zerbes RM, van der Laan M, Pfanner N. Role of the mitochondrial contact site and cristae organizing system in membrane architecture and dynamics. *Biochimica et Biophysica Acta (BBA)-Molecular Cell Research*. 2017;1864:737–746.

13. Hu C, Shu L, Huang X, Yu J, Gong L, Yang M, Wu Z, Gao Z, Zhao Y, Chen L. OPA1 and MICOS Regulate mitochondrial crista dynamics and formation. *Cell death & disease*. 2020;11:1–17.

14. Friedman JR, Mourier A, Yamada J, McCaffery JM, Nunnari J. MICOS coordinates with respiratory complexes and lipids to establish mitochondrial inner membrane architecture. *Elife*. 2015;4:e07739.

15. Glancy B, Kim Y, Katti P, Willingham TB. The Functional Impact of Mitochondrial Structure Across Subcellular Scales. *Front Physiol*. 2020;11:541040.

16. Willingham TB, Ajayi PT, Glancy B. Subcellular Specialization of Mitochondrial Form and Function in Skeletal Muscle Cells. *Front Cell Dev Biol*. 2021;9:757305.

17. Vincent AE, White K, Davey T, Philips J, Ogden RT, Lawless C, Warren C, Hall MG, Ng YS, Falkous G. Quantitative 3D mapping of the human skeletal muscle mitochondrial network. *Cell reports*. 2019;26:996–1009.

18. Faitg J, Lacefield C, Davey T, White K, Laws R, Kosmidis S, Reeve AK, Kandel ER, Vincent AE, Picard M. 3D Neuronal Mitochondrial Morphology in Axons, Dendrites, and Somata of the Aging Mouse Hippocampus. *bioRxiv*. 2021.

19. Bratic A, Larsson N-G. The role of mitochondria in aging. *The Journal of clinical investigation*. 2013;123:951–957.

20. Barja G. The mitochondrial free radical theory of aging. *Progress in molecular biology and translational science*. 2014;127:1–27.

21. Rowland AA, Voeltz GK. Endoplasmic reticulum–mitochondria contacts: function of the junction. *Nature reviews Molecular cell biology*. 2012;13:607–615.

22. Renken CW. The structure of mitochondria. 2004.

23. Kühlbrandt W. Structure and function of mitochondrial membrane protein complexes. *BMC biology*. 2015;13:1–11.

24. Vendelin M, Béraud N, Guerrero K, Andrienko T, Kuznetsov AV, Olivares J, Kay L, Saks VA. Mitochondrial regular arrangement in muscle cells: a “crystal-like” pattern. *American Journal of Physiology-Cell Physiology*. 2005;288:C757–C767.

25. Koopman WJH, Visch H-J, Verkaart S, van den Heuvel LWPJ, Smeitink JAM, Willems PHGM. Mitochondrial network complexity and pathological decrease in complex I activity are tightly correlated in isolated human complex I deficiency. *Am J Physiol Cell Physiol*. 2005;289:C881-890.

26. Zheng J, Croteau DL, Bohr VA, Akbari M. Diminished OPA1 expression and impaired mitochondrial morphology and homeostasis in Aprataxin-deficient cells. *Nucleic acids research*. 2019;47:4086–4110.

27. Varanita T, Soriano ME, Romanello V, Zaglia T, Quintana-Cabrera R, Semenzato M, Menabò R, Costa V, Civiletto G, Pesce P. The OPA1-dependent mitochondrial cristae remodeling pathway controls atrophic, apoptotic, and ischemic tissue damage. *Cell metabolism*. 2015;21:834–844.

28. Li H, Ruan Y, Zhang K, Jian F, Hu C, Miao L, Gong L, Sun L, Zhang X, Chen S. Mic60/Mitofilin determines MICOS assembly essential for mitochondrial dynamics and mtDNA nucleoid organization. *Cell Death & Differentiation*. 2016;23:380–392.

29. Lam J, Katti P, Biete M, Mungai M, AshShareef S, Neikirk K, Lopez EG, Vue Z, Christensen TA, Beasley HK. A Universal Approach to Analyzing Transmission Electron Microscopy with ImageJ. *bioRxiv*. 2021.

30. Hinton A, Katti P, Christensen TA, Mungai M, Shao J, Zhang L, Trushin S, Alghanem A, Jaspersen A, Geroux RE. A comprehensive approach for artifact-free sample preparation and assessment of mitochondrial morphology in tissue and cultured cells. *bioRxiv*. 2021.

31. Pereira RO, Tadinada SM, Zasadny FM, Oliveira KJ, Pires KMP, Olvera A, Jeffers J, Souvenir R, Mcglauflin R, Seei A. OPA 1 deficiency promotes secretion of FGF 21 from muscle that prevents obesity and insulin resistance. *The EMBO journal*. 2017;36:2126–2145.

32. John GB, Shang Y, Li L, Renken C, Mannella CA, Selker JM, Rangell L, Bennett MJ, Zha J. The mitochondrial inner membrane protein mitofilin controls cristae morphology. *Molecular biology of the cell*. 2005;16:1543–1554.

33. Ding C, Wu Z, Huang L, Wang Y, Xue J, Chen S, Deng Z, Wang L, Song Z, Chen S. Mitofilin and CHCHD6 physically interact with Sam50 to sustain cristae structure. *Scientific reports*. 2015;5:1–11.

34. Darshi M, Taylor SS. Mitochondrial ChChD3 acts as a Scaffold for Mitofilin, Sam50 and PKA. 2008.

35. An J, Shi J, He Q, Lui K, Liu Y, Huang Y, Sheikh MS. CHCM1/CHCHD6, novel mitochondrial protein linked to regulation of mitofilin and mitochondrial cristae morphology. *Journal of Biological Chemistry*. 2012;287:7411–7426.

36. Ott C, Dorsch E, Fraunholz M, Straub S, Kozjak-Pavlovic V. Detailed analysis of the human mitochondrial contact site complex indicate a hierarchy of subunits. *PloS one*. 2015;10:e0120213.

37. Kondadi AK, Anand R, Reichert AS. Functional interplay between cristae biogenesis, mitochondrial dynamics and mitochondrial DNA integrity. *International journal of molecular sciences*. 2019;20:4311.

38. Stephan T, Brüser C, Deckers M, Steyer AM, Balzarotti F, Barbot M, Behr TS, Heim G, Hübner W, Ilgen P. MICOS assembly controls mitochondrial inner membrane remodeling and crista junction redistribution to mediate cristae formation. *The EMBO journal*. 2020;39:e104105.

39. Wang L, Hsu T, Lin H, Fu C. Drosophila MICOS knockout impairs mitochondrial structure and function and promotes mitophagy in muscle tissue. *Biology Open*. 2020;9:bio054262.

40. Torres MJ, Kew KA, Ryan TE, Pennington ER, Lin C-T, Buddo KA, Fix AM, Smith CA, Gilliam LA, Karvinen S, Lowe DA, Spangenburg EE, Zeczycki TN, Shaikh SR, Neufer PD. 17β-Estradiol Directly Lowers Mitochondrial Membrane Microviscosity and Improves Bioenergetic Function in Skeletal Muscle. *Cell Metabolism*. 2018;27:167-179.e7.

41. Kitajima Y, Ono Y. Estrogens maintain skeletal muscle and satellite cell functions. *Journal of Endocrinology*. 2016;229:267–275.

42. Wasilewski M, Semenzato M, Rafelski SM, Robbins J, Bakardjiev AI, Scorrano L. Optic Atrophy 1-Dependent Mitochondrial Remodeling Controls Steroidogenesis in Trophoblasts. *Current Biology*. 2012;22:1228–1234.

43. Sarzi E, Seveno M, Angebault C, Milea D, Rönnbäck C, Quilès M, Adrian M, Grenier J, Caignard A, Lacroux A, Lavergne C, Reynier P, Larsen M, Hamel CP, Delettre C, Lenaers G, Müller A. Increased steroidogenesis promotes early-onset and severe vision loss in females with OPA1 dominant optic atrophy. *Human Molecular Genetics*. 2016;25:2539–2551.

44. Chao de la Barca JM, Fogazza M, Rugolo M, Chupin S, Del Dotto V, Ghelli AM, Carelli V, Simard G, Procaccio V, Bonneau D, Lenaers G, Reynier P, Zanna C. Metabolomics hallmarks OPA1 variants correlating with their in vitro phenotype and predicting clinical severity. *Hum Mol Genet*. 2020;29:1319–1329.

45. Dahl R, Larsen S, Dohlmann TL, Qvortrup K, Helge JW, Dela F, Prats C. Three-dimensional reconstruction of the human skeletal muscle mitochondrial network as a tool to assess mitochondrial content and structural organization. *Acta Physiol (Oxf)*. 2015;213:145–155.

46. Glancy B, Hartnell LM, Malide D, Yu Z-X, Combs CA, Connelly PS, Subramaniam S, Balaban RS. Mitochondrial reticulum for cellular energy distribution in muscle. *Nature*. 2015;523:617–620.

47. Garnier A, Fortin D, Delomenie C, Momken I, Veksler V, Ventura□Clapier R. Depressed mitochondrial transcription factors and oxidative capacity in rat failing cardiac and skeletal muscles. *The Journal of physiology*. 2003;551:491–501.

48. Mukund K, Subramaniam S. Skeletal muscle: A review of molecular structure and function, in health and disease. *Wiley Interdisciplinary Reviews: Systems Biology and Medicine*. 2020;12:e1462.

49. Lin I-H, Chang J-L, Hua K, Huang W-C, Hsu M-T, Chen Y-F. Skeletal muscle in aged mice reveals extensive transformation of muscle gene expression. *BMC genetics*. 2018;19:1–13.

50. Sanz A, Stefanatos RK. The mitochondrial free radical theory of aging: a critical view. *Current aging science*. 2008;1:10–21.

51. Rolo AP, Palmeira CM. Diabetes and mitochondrial function: role of hyperglycemia and oxidative stress. *Toxicology and applied pharmacology*. 2006;212:167–178.

52. Lavorato M, Iyer VR, Dewight W, Cupo RR, Debattisti V, Gomez L, Fuente SD la, Zhao Y-T, Valdivia HH, Hajnóczky G, Franzini-Armstrong C. Increased mitochondrial nanotunneling activity, induced by calcium imbalance, affects intermitochondrial matrix exchanges. *PNAS*. 2017;114:E849–E858.

53. Cefalu WT, Wang ZQ, Werbel S, Bell-Farrow A, Crouse JR, Hinson WH, Terry JG, Anderson R. Contribution of visceral fat mass to the insulin resistance of aging. *Metabolism*. 1995;44:954–959.

54. Liu T, Woo JA, Bukhari MZ, LePochat P, Chacko A, Selenica MB, Yan Y, Kotsiviras P, Buosi SC, Zhao X. CHCHD10□regulated OPA1□mitofilin complex mediates TDP□43□induced mitochondrial phenotypes associated with frontotemporal dementia. *The FASEB Journal*. 2020;34:8493–8509.

55. de La Barca JMC, Arrázola MS, Bocca C, Arnauné-Pelloquin L, Iuliano O, Tcherkez G, Lenaers G, Simard G, Belenguer P, Reynier P. The metabolomic signature of Opa1 deficiency in rat primary cortical neurons shows aspartate/glutamate depletion and phospholipids remodeling. *Scientific reports*. 2019;9:1–8.

56. Bocca C, Nzoughet JK, Leruez S, Amati-Bonneau P, Ferré M, Kane M-S, Veyrat-Durebex C, de La Barca JMC, Chevrollier A, Homedan C. A plasma metabolomic signature involving purine metabolism in human optic atrophy 1 (OPA1)-related disorders. *Investigative ophthalmology & visual science*. 2018;59:185–195.

57. de La Barca JMC, Simard G, Sarzi E, Chaumette T, Rousseau G, Chupin S, Gadras C, Tessier L, Ferré M, Chevrollier A. Targeted metabolomics reveals early dominant optic atrophy signature in optic nerves of Opa1delTTAG/+ mice. *Investigative ophthalmology & visual science*. 2017;58:812–820.

58. Garcia-Cazarin ML, Snider NN, Andrade FH. Mitochondrial isolation from skeletal muscle. *JoVE (Journal of Visualized Experiments)*. 2011;:e2452.

59. Wortel IMN, van der Meer LT, Kilberg MS, van Leeuwen FN. Surviving Stress: Modulation of ATF4-Mediated Stress Responses in Normal and Malignant Cells. *Trends Endocrinol Metab*. 2017;28:794–806.

60. Cristae undergo continuous cycles of membrane remodelling in a MICOS-dependent manner. *EMBO reports*. 2020;21:e49776.

61. Hessenberger M, Zerbes RM, Rampelt H, Kunz S, Xavier AH, Purfürst B, Lilie H, Pfanner N, van der Laan M, Daumke O. Regulated membrane remodeling by Mic60 controls formation of mitochondrial crista junctions. *Nat Commun*. 2017;8:15258.

62. Tarasenko D, Barbot M, Jans DC, Kroppen B, Sadowski B, Heim G, Möbius W, Jakobs S, Meinecke M. The MICOS component Mic60 displays a conserved membrane-bending activity that is necessary for normal cristae morphology. *J Cell Biol*. 2017;216:889–899.

63. Rieusset J. The role of endoplasmic reticulum-mitochondria contact sites in the control of glucose homeostasis: an update. *Cell death & disease*. 2018;9:1–12.

64. Han J, Back SH, Hur J, Lin Y-H, Gildersleeve R, Shan J, Yuan CL, Krokowski D, Wang S, Hatzoglou M. ER-stress-induced transcriptional regulation increases protein synthesis leading to cell death. *Nature cell biology*. 2013;15:481–490.

65. Rampelt H, Wollweber F, Licheva M, de Boer R, Perschil I, Steidle L, Becker T, Bohnert M, van der Klei I, Kraft C, van der Laan M, Pfanner N. Dual role of Mic10 in mitochondrial

cristae organization and ATP synthase-linked metabolic adaptation and respiratory growth. *Cell Reports*. 2022;38:110290.

66. Darshi M, Mendiola VL, Mackey MR, Murphy AN, Koller A, Perkins GA, Ellisman MH, Taylor SS. ChChd3, an inner mitochondrial membrane protein, is essential for maintaining crista integrity and mitochondrial function. *Journal of biological chemistry*. 2011;286:2918–2932.

67. Piñero-Martos E, Ortega-Vila B, Pol-Fuster J, Cisneros-Barroso E, Ruiz-Guerra L, Medina-Dols A, Heine-Suñer D, Lladó J, Olmos G, Vives-Bauzà C. Disrupted in schizophrenia 1 (DISC1) is a constituent of the mammalian mitochondrial contact site and cristae organizing system (MICOS) complex, and is essential for oxidative phosphorylation. *Human Molecular Genetics*. 2016;25:4157–4169.

68. Genin EC, Plutino M, Bannwarth S, Villa E, Cisneros□Barroso E, Roy M, Ortega□Vila B, Fragaki K, Lespinasse F, Pinero□Martos E. CHCHD 10 mutations promote loss of mitochondrial cristae junctions with impaired mitochondrial genome maintenance and inhibition of apoptosis. *EMBO molecular medicine*. 2016;8:58–72.

69. Park Y-U, Jeong J, Lee H, Mun JY, Kim J-H, Lee JS, Nguyen MD, Han SS, Suh P-G, Park SK. Disrupted-in-schizophrenia 1 (DISC1) plays essential roles in mitochondria in collaboration with Mitofilin. *Proceedings of the National Academy of Sciences*. 2010;107:17785–17790.

70. Genin EC, Bannwarth S, Lespinasse F, Ortega-Vila B, Fragaki K, Itoh K, Villa E, Lacas-Gervais S, Jokela M, Auranen M, Ylikallio E, Mauri-Crouzet A, Tyynismaa H, Vihola A, Augé G, Cochaud C, Sesaki H, Ricci J-E, Udd B, Vives-Bauza C, Paquis-Flucklinger V. Loss of MICOS complex integrity and mitochondrial damage, but not TDP-43 mitochondrial localisation, are likely associated with severity of CHCHD10-related diseases. *Neurobiology of Disease*. 2018;119:159–171.

71. Bannwarth S, Ait-El-Mkadem S, Chaussenot A, Genin EC, Lacas-Gervais S, Fragaki K, Berg-Alonso L, Kageyama Y, Serre V, Moore DG, Verschueren A, Rouzier C, Le Ber I, Augé G, Cochaud C, Lespinasse F, N'Guyen K, de Septenville A, Brice A, Yu-Wai-Man P, Sesaki H, Pouget J, Paquis-Flucklinger V. A mitochondrial origin for frontotemporal dementia and amyotrophic lateral sclerosis through CHCHD10 involvement. *Brain*. 2014;137:2329–2345.

72. Eramo MJ, Lisnyak V, Formosa LE, Ryan MT. The 'mitochondrial contact site and cristae organising system' (MICOS) in health and human disease. *The Journal of Biochemistry*. 2020;167:243–255.

73. Martin CR, Preedy VR, Rajendram R. Assessments, Treatments and Modeling in Aging and Neurological Disease: The Neuroscience of Aging. Academic Press; 2021: 1-608.

74. Kandlur A, Satyamoorthy K, Gangadharan G. Oxidative Stress in Cognitive and Epigenetic Aging: A Retrospective Glance. *Frontiers in Molecular Neuroscience*. 2020;13. Available at https://www.frontiersin.org/article/10.3389/fnmol.2020.00041. Accessed March 17, 2022.

75. Pereira RO, Marti A, Olvera AC, Tadinada SM, Bjorkman SH, Weatherford ET, Morgan DA, Westphal M, Patel PH, Kirby AK. OPA1 deletion in brown adipose tissue improves thermoregulation and systemic metabolism via FGF21. *Elife*. 2021;10:e66519.

76. Boudina S, Sena S, Theobald H, Sheng X, Wright JJ, Hu XX, Aziz S, Johnson JI, Bugger H, Zaha VG, Abel ED. Mitochondrial energetics in the heart in obesity-related diabetes: direct evidence for increased uncoupled respiration and activation of uncoupling proteins. *Diabetes*. 2007;56:2457–2466.

77. Garza-Lopez E, Vue Z, Katti P, Neikirk K, Biete M, Lam J, Beasley HK, Marshall AG, Rodman TA, Christensen TA, Salisbury JL, Vang L, Mungai M, AshShareef S, Murray SA, Shao J, Streeter J, Glancy B, Pereira RO, Abel ED, Hinton A. Protocols for Generating Surfaces and Measuring 3D Organelle Morphology Using Amira. *Cells*. 2022;11:65.

78. Neikirk K, Vue Z, Katti P, Shao J, Christensen TA, Lopez EG, Marshall A, Palavicino-Maggio C, Ponce J, Alghanem A. Systematic Transmission Electron Microscopy-Based Identification of Cellular Degradation Machinery. *bioRxiv*. 2021.

79. Li B, Tang J, Yang Q, Li S, Cui X, Li Y, Chen Y, Xue W, Li X, Zhu F. NOREVA: normalization and evaluation of MS-based metabolomics data. *Nucleic acids research*. 2017;45:W162–W170.

80. Cantor JR, Abu-Remaileh M, Kanarek N, Freinkman E, Gao X, Louissaint Jr A, Lewis CA, Sabatini DM. Physiologic medium rewires cellular metabolism and reveals uric acid as an endogenous inhibitor of UMP synthase. *Cell*. 2017;169:258–272.

81. Chong J, Soufan O, Li C, Caraus I, Li S, Bourque G, Wishart DS, Xia J. MetaboAnalyst 4.0: towards more transparent and integrative metabolomics analysis. *Nucleic acids research*. 2018;46:W486–W494.

82. Phillips MA, Arnold KR, Vue Z, Beasley HK, Garza-Lopez E, Marshall AG, Morton DJ, McReynolds MR, Barter TT, Hinton A. Combining Metabolomics and Experimental Evolution Reveals Key Mechanisms Underlying Longevity Differences in Laboratory Evolved Drosophila melanogaster Populations. *International Journal of Molecular Sciences*. 2022;23:1067.

83. Wende AR, O'Neill BT, Bugger H, Riehle C, Tuinei J, Buchanan J, Tsushima K, Wang L, Caro P, Aili G, Sloan C, Kim BJ, Wang X, Pereira RO, McCrory MA, Nye BG, Benavides GA, Darley-Usmar VM, Shioi T, Weimer BC, Abela ED. Enhanced cardiac Akt/protein kinase B signaling contributes to pathological cardiac hypertrophy in part by impairing mitochondrial function via transcriptional repression of mitochondrion-targeted nuclear genes. *Molecular and Cellular Biology*. 2015;35:831–846.

(13) **SUPPORTING INFORMATION**

(14) TABLES

(15) FIGURE LEGEND

Figure 1: Decreased mitochondrial size and volume in skeletal muscle and cardiac muscle of aged mice in SBF-SEM 3D reconstructions.

(**A-C**) Representative SBF-SEM orthoslice for skeletal muscle. (**A'-C'**) 3D reconstructions of mitochondria (various colors) in skeletal muscle mouse tissues of different ages overlaid on ortho slices. (**A''-C''**) 3D reconstructed and isolated mitochondria for clear visualization. (**A'-C''**) Pseudo-colored individual mitochondria in skeletal muscle to differentiate micro-level changes. (**A, A', A''**) The 2D ortho slice, the overlay of the 2D ortho slice, and the 3D reconstruction with individually colored mitochondria in tissue from 3-month-old mice. (**B, B', B''**) The 2D ortho slice, the overlay of the 2D ortho slice, and the 3D reconstruction with individually colored mitochondria in tissue from 1-year-old mice. (**C, C', C''**) The 2D ortho slice, the overlay of the 2D ortho slice, and the 3D reconstruction with individually colored mitochondria in tissue from 2-year-old mice. (**D-F**) Representative SBF-SEM orthoslice for cardiac muscle. (**D'-F'**) 3D reconstructions of mitochondria in mouse tissues of different ages overlaid on ortho slices. (**D''-F''**) 3D reconstructed and isolated mitochondria for clear visualization. (**G-J**) Quantification of 3D reconstructions. (**G, H**) Mitochondrial area and perimeter in cardiac and skeletal tissues of different ages. (**I**) Sphericity of mitochondria in cardiac and skeletal muscle of different ages. (**J**) Mitochondrial volume in cardiac and skeletal muscle of different ages. Significance values **** indicates $p \leq 0.0001$, respectively.

Figure 2: SBF-SEM 3D reconstruction in skeletal muscle and cardiac of aged mice
(**A-C**) 3D reconstruction of individually colored mitochondria from a transverse view for mouse skeletal tissues of different ages. (**A'-C'**) 3D reconstruction of individually colored mitochondria from a longitudinal view in skeletal muscle tissues of different ages. (**D-F**) 3D reconstruction of individually colored mitochondria from a transverse view for mouse cardiac muscle of different ages. (**D'-F'**) 3D reconstruction of individually colored mitochondria from a longitudinal view in cardiac muscle tissues of different ages. (**G**) Representative examples of 3D reconstruction of mitochondria in skeletal muscle of different ages organized by volume. (**H**) Representative examples of 3D reconstruction of mitochondria in cardiac muscle of different ages organized by volume. (**I**) MCI for mitochondria in tissues of different ages. Significance values **** indicates $p \leq 0.0001$, respectively.

Figure 3. Mitochondrial nanotunnels in skeletal mouse tissue.
(**A-C**) TEM tracing showing identified nanotunnels across aged cohorts in skeletal mouse tissue. (**D**) Representative examples of 3D reconstruction of nanotunnels in tissues of different ages organized by volume. (**E-H**) Quantification comparing frequency, average nanotunnel amount, nanotunnel length, and diameter of nanotunnels, respectively, across aged cohorts. (**I**) Histogram showing frequency of various nanotunnel lengths for each age group. (**J**) Histogram showing frequency of various nanotunnel diameters for each age group. **, **** indicate $p \leq 0.01$, and $p \leq 0.0001$, respectively.

Figure 4. Knockout of MICOS complex proteins or *Opa-1* in myotubes results in changes in mitochondria, cristae, and oxygen consumption rates.
(**A-C**) Representative images of mitochondria and cristae from myotubes of OPA-1 and *Mitofilin* knockout mice compared to WT. (**P-S**) Representative images of mitochondria and cristae from myotubes of *Opa-1*, *CHCHD3*, and *CHCHD6* knockout mice compared to WT. (**D, T**) Mitochondrial area in myotubes of *Opa-1*, *CHCHD3*, *CHCHD6*, and *Mitofilin* knockout mice compared to WT. (**E, U**) Circularity index, measuring the roundness and symmetry of

mitochondria, in myotubes of *Opa-1*, *CHCHD3*, *CHCHD6*, and *Mitofilin* knockout mice compared to WT. (**F, V**) The number of mitochondria in myotubes of *Opa-1*, *CHCHD3*, *CHCHD6*, and *Mitofilin* knockout mice compared to WT. (**W, G**) Quantification of individual cristae in myotubes of *Opa-1*, *CHCHD3*, *CHCHD6*, and *Mitofilin* knockout mice compared to WT. (**H, X**) Cristae scores measuring the uniformity and idealness of cristae in myotubes of *Opa-1*, *CHCHD3*, *CHCHD6*, and *Mitofilin* knockout mice compared to WT. (**I, Y**) Surface area of the average cristae in myotubes of *Opa-1*, *CHCHD3*, *CHCHD6*, and *Mitofilin* knockout mice compared to WT. (**J, Z**) OCR in myotubes of *Opa-1*, *CHCHD3*, *CHCHD6*, and *Mitofilin* knockout mice compared to WT. **(K, AA)** Basal OCR, the net respiration rate once non-mitochondrial respiration has been removed, in myotubes of *Opa-1*, *CHCHD3*, *CHCHD6*, and *Mitofilin* knockout mice compared to WT. (**L, AB**) ATP-linked respiration, shown from intervals 4−7 in the OCR graphs, was determined by the addition of oligomycin (an inhibitor of respiration), thus representing the respiration dependent on ATP, in myotubes of *Opa-1*, *CHCHD3*, *CHCHD6*, and *Mitofilin* knockout mice compared to WT. (**M, AC**) Maximum OCR, represented by the peak from intervals 7−11 once non-mitochondrial respiration was deducted, in myotubes of *Opa-1*, *CHCHD3*, *CHCHD6*, and *Mitofilin* knockout mice compared to WT. (**N, AD**) The reserve capacity, which is represented by the difference between basal OCR and maximum OCR, in myotubes of *Opa-1*, *CHCHD3*, *CHCHD6*, and *Mitofilin* knockout mice compared to WT. (**O, AE**) Proton leak, representing non-phosphorylating electron transfer, in myotubes of *Opa-1*, *CHCHD3*, *CHCHD6*, and *Mitofilin* knockout mice compared to WT. Significance values *, **, ***, **** indicate $p \leq 0.05$, $p \leq 0.01$, $p \leq 0.001$, and $p \leq 0.0001$, respectively.

Figure 5. Loss of OPA-1 or MICOS complex proteins in myotubes decreases mitochondrial size and length.
(**A-C**) Representative images showing 3D reconstructions of mitochondria in myotubes of *Opa-1* and *Mitofilin* knockout mice compared to WT. (**D**) Mitochondrial 3D length in myotubes of *Opa-1* and *Mitofilin* knockout mice compared to WT. (**E**) Volume of mitochondria in myotubes of *Opa-1* and *Mitofilin* knockout mice compared to WT. (**F-I**) Representative images showing 3D reconstruction of mitochondria in myotubes of *Opa-1***,** *CHCHD3*, and *CHCHD6* knockout mice compared to WT. (**J**) Mitochondrial 3D length in myotubes of *Opa-1***,** *CHCHD3*, and *CHCHD6* knockout mice compared to WT. (**K**) Mitochondrial volume in myotubes of *Opa-1***,** *CHCHD3*, and *CHCHD6* knockout mice compared to WT. Significance value **** indicates $p \leq 0.0001$.

Figure 6. Metabolomics of myotubes lacking components of the MICOS complex. (**A**) Metabolite PCA for myotubes of *Mitofilin* knockout mice compared to control. (**B**) T-test comparing control to *Mitofilin* knockout mice. (**C**) Heatmap showing the relative abundance of ions for control and *Mitofilin* knockout mice. (**D**) Enrichment analysis of metabolites, which links together several similarly functioning metabolites, with the relative abundance for *Mitofilin* knockout mice. (**E**) PCA for *CHCHD6* and *CHCHD3* knockout mice compared to control. (**F**) ANOVA test comparing control to *CHCHD3* and *CHCHD6* knockout mice. (**G**) Heatmap showing the relative abundance of ions for control, *CHCHD3*, and *CHCHD6* knockout mice. (**H**) Enrichment analysis metabolite, which links together several similarly functioning metabolites, with the relative abundance for *CHCHD3* and *CHCHD6* knockout mice.

Supplementary Figure 1. Decreased mitochondrial size and volume in skeletal muscle and cardiac muscle of aged mice in SBF-SEM 3D reconstructions. (**A-C**) In skeletal muscle and (**D-F**), a decrease in perimeter, 3D area, and volume 3D are observed. Significance values *, **, ***, **** indicate $p \leq 0.05$, $p \leq 0.01$, $p \leq 0.001$, and $p \leq 0.0001$, respectively.

Supplementary Figure 2. Sphericity changes across aging in (**A**) skeletal muscle and (**B**) cardiac muscle. Significance value **** indicates $p \leq 0.0001$.

Supplementary Figure 3. Transcription of *Opa-1* and MICOS genes in aging mouse muscle. (**A-D**) Fold changes in the amount of OPA-1 and MICOS gene transcripts in mitochondria of myocytes of 3-month-old, 1-year-old, and 2-year-old mice as measured by RT-qPCR. (**A**) *Opa-1* transcripts. (**B**) *Mitofilin* transcripts. (**C**) *CHCHD3* transcripts. (**D**) *CHCHD6* transcripts. Significance values *, **, ***, **** indicate $p \leq 0.05$, $p \leq 0.01$, $p \leq 0.001$, and $p \leq 0.0001$, respectively.

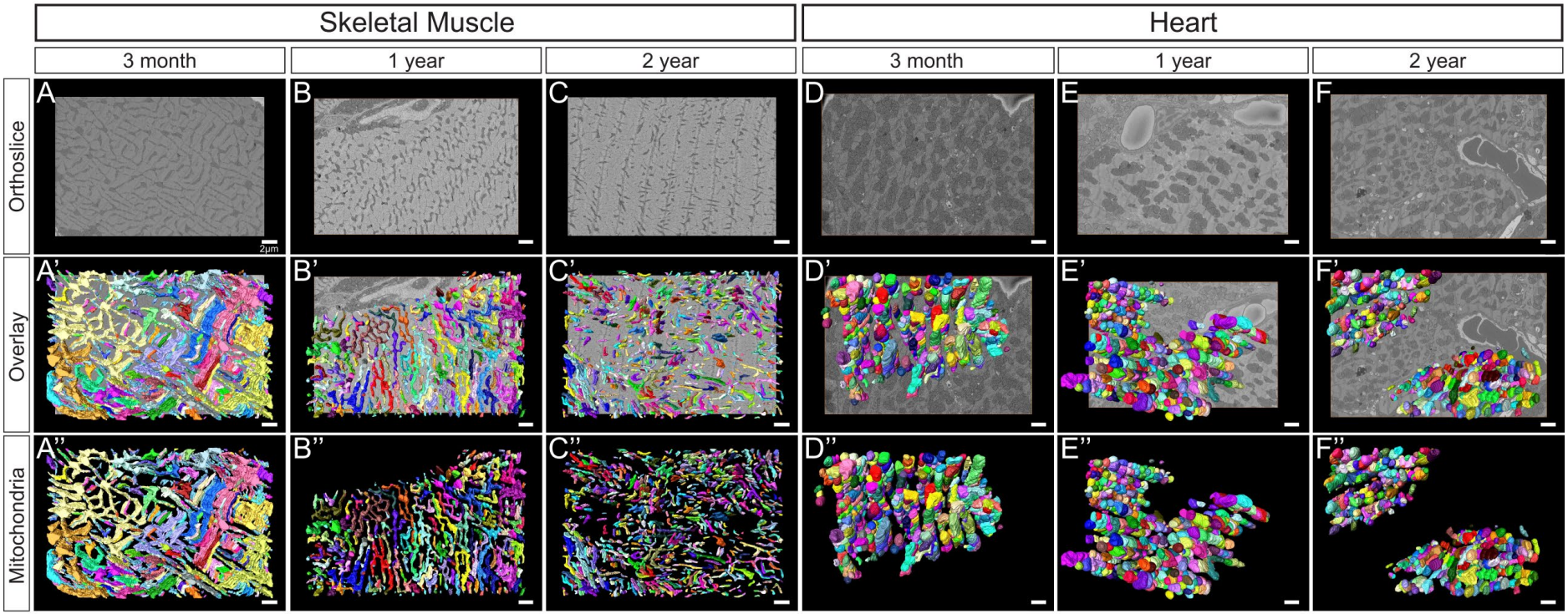
Skeletal Muscle
Heart
3 month
1 year
2 year
3 month
1 year
2 year
Orthoslice
Overlay
Mitochondria
A
B
C
D
E
F
2µm
A'
B'
C'
D'
E'
F'
A''
B''
C''
D''
E''
F''

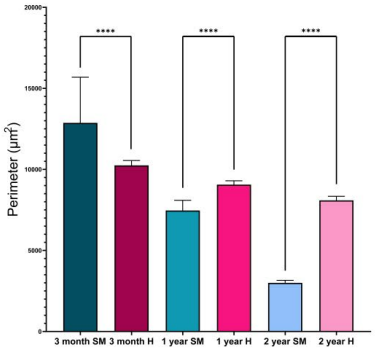
G
Perimeter (µm²)
20000
15000
10000
5000
0
****
****
****
3 month SM
3 month H
1 year SM
1 year H
2 year SM
2 year H

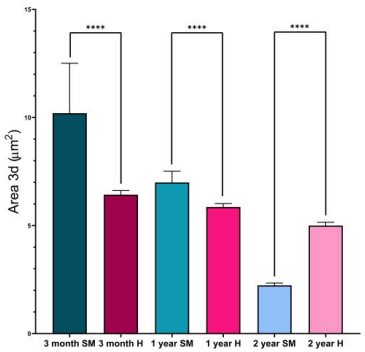
H
Area 3d (µm²)
15
10
5
0
****
****
****
3 month SM
3 month H
1 year SM
1 year H
2 year SM
2 year H

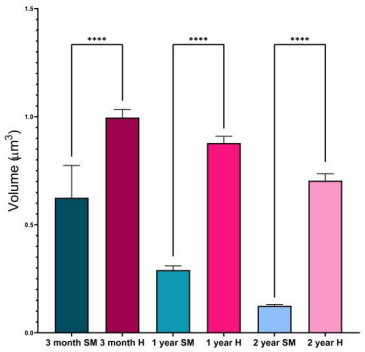
I
Volume (µm³)
1.5
1.0
0.5
0.0
****
****
****
3 month SM
3 month H
1 year SM
1 year H
2 year SM
2 year H

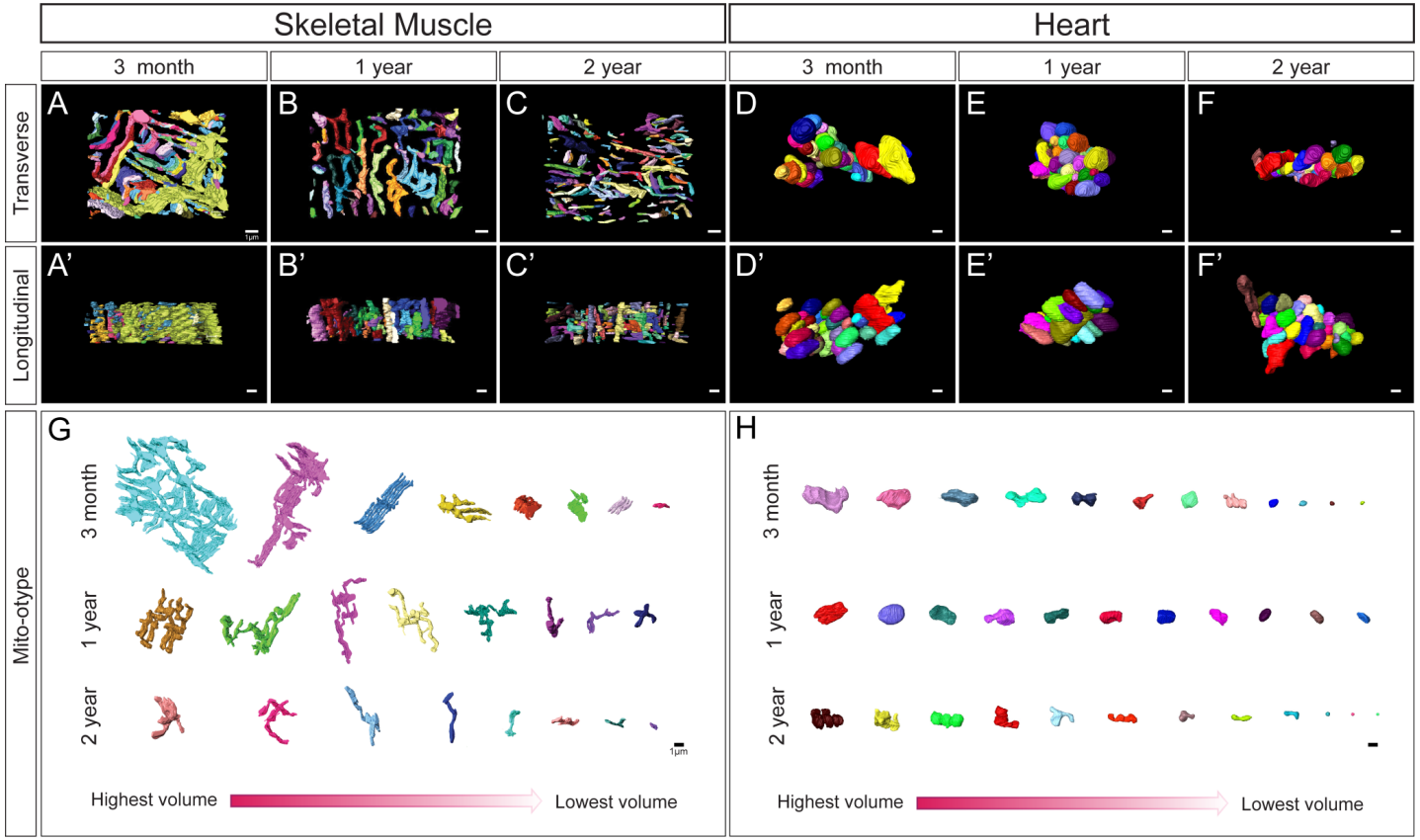
Skeletal Muscle
Heart
3 month
1 year
2 year
3 month
1 year
2 year
Transverse
Longitudinal
Mito-otype
A
B
C
D
E
F
A'
B'
C'
D'
E'
F'
G
H
3 month
1 year
2 year
Highest volume
Lowest volume
Highest volume
Lowest volume

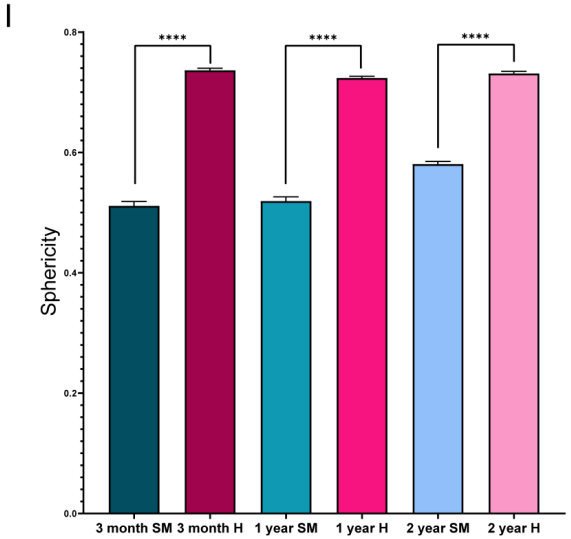
I
Sphericity
0.0
0.2
0.4
0.6
0.8
****
****
****
3 month SM
3 month H
1 year SM
1 year H
2 year SM
2 year H

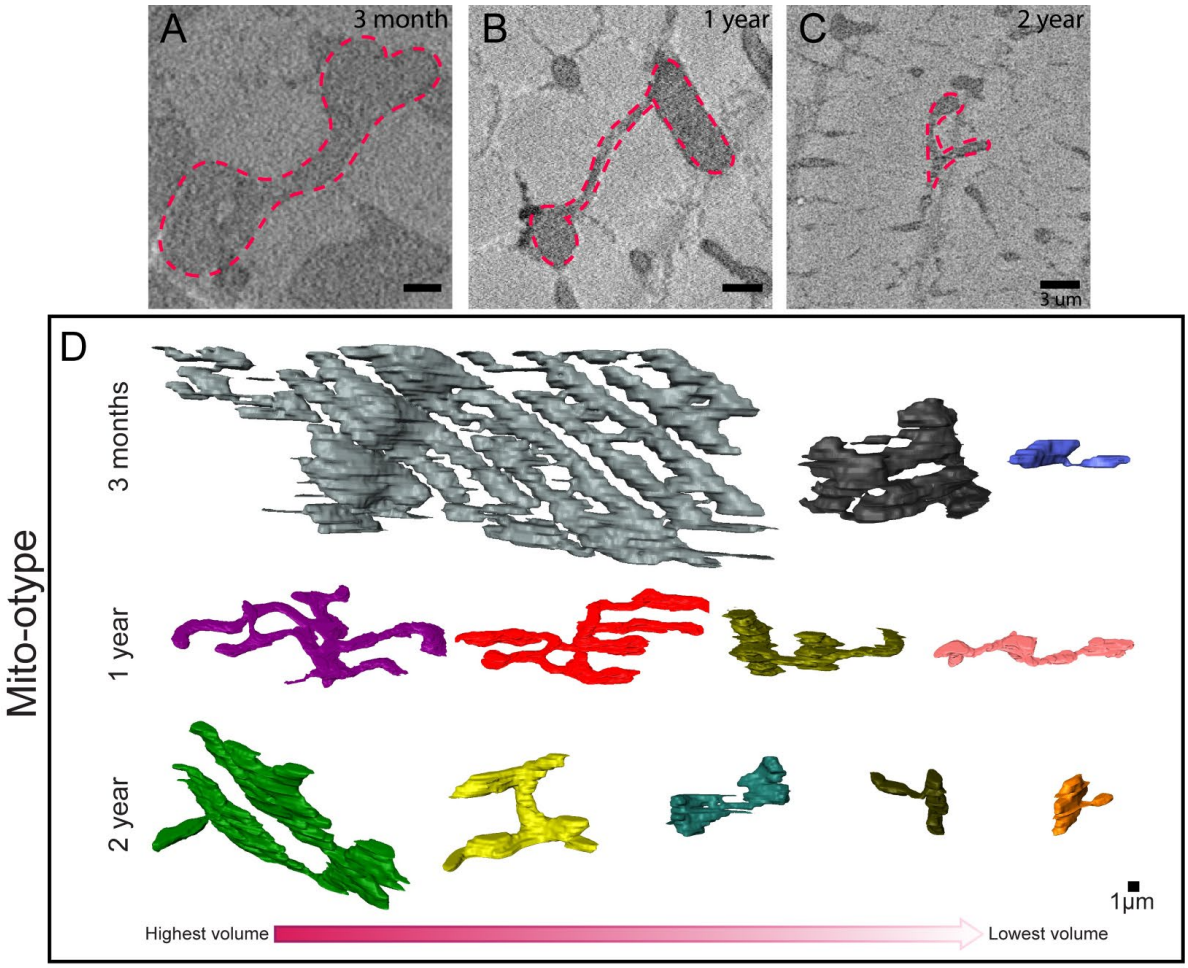
A
3 month
B
1 year
C
2 year
3 µm
D
Mito-otype
3 months
1 year
2 year
1µm
Highest volume
Lowest volume

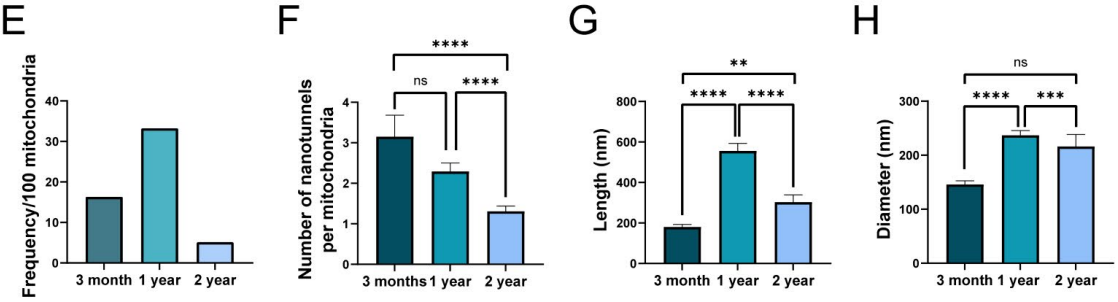
E
Frequency/100 mitochondria
3 month
1 year
2 year
F
Number of nanotunnels per mitochondria
ns
****
****
3 months
1 year
2 year
G
Length (nm)
**
****
****
3 month
1 year
2 year
H
Diameter (nm)
ns
****
***
3 month
1 year
2 year

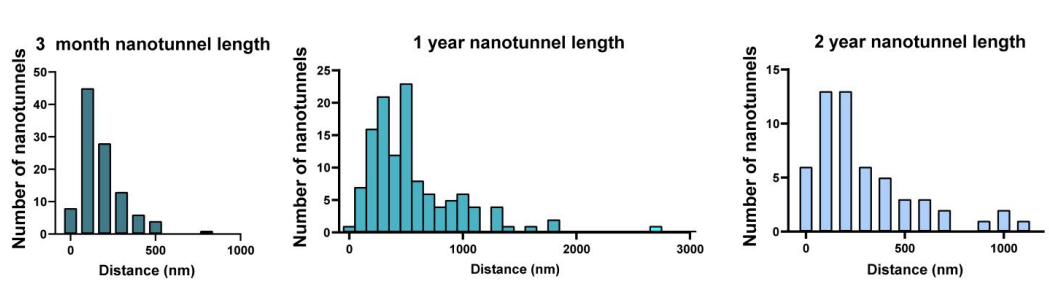
I
3 month nanotunnel length
1 year nanotunnel length
2 year nanotunnel length
Number of nanotunnels
Distance (nm)

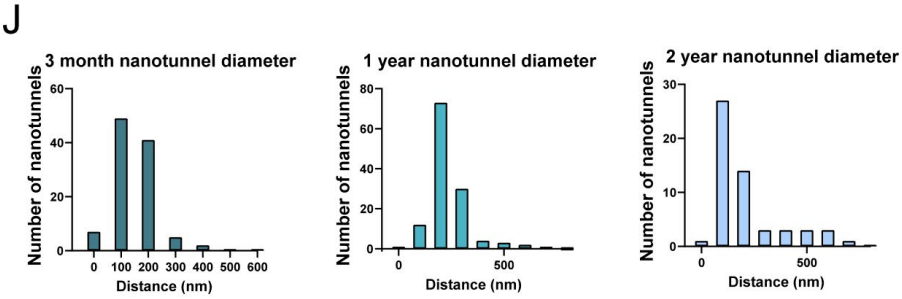
J
3 month nanotunnel diameter
1 year nanotunnel diameter
2 year nanotunnel diameter
Number of nanotunnels
Distance (nm)

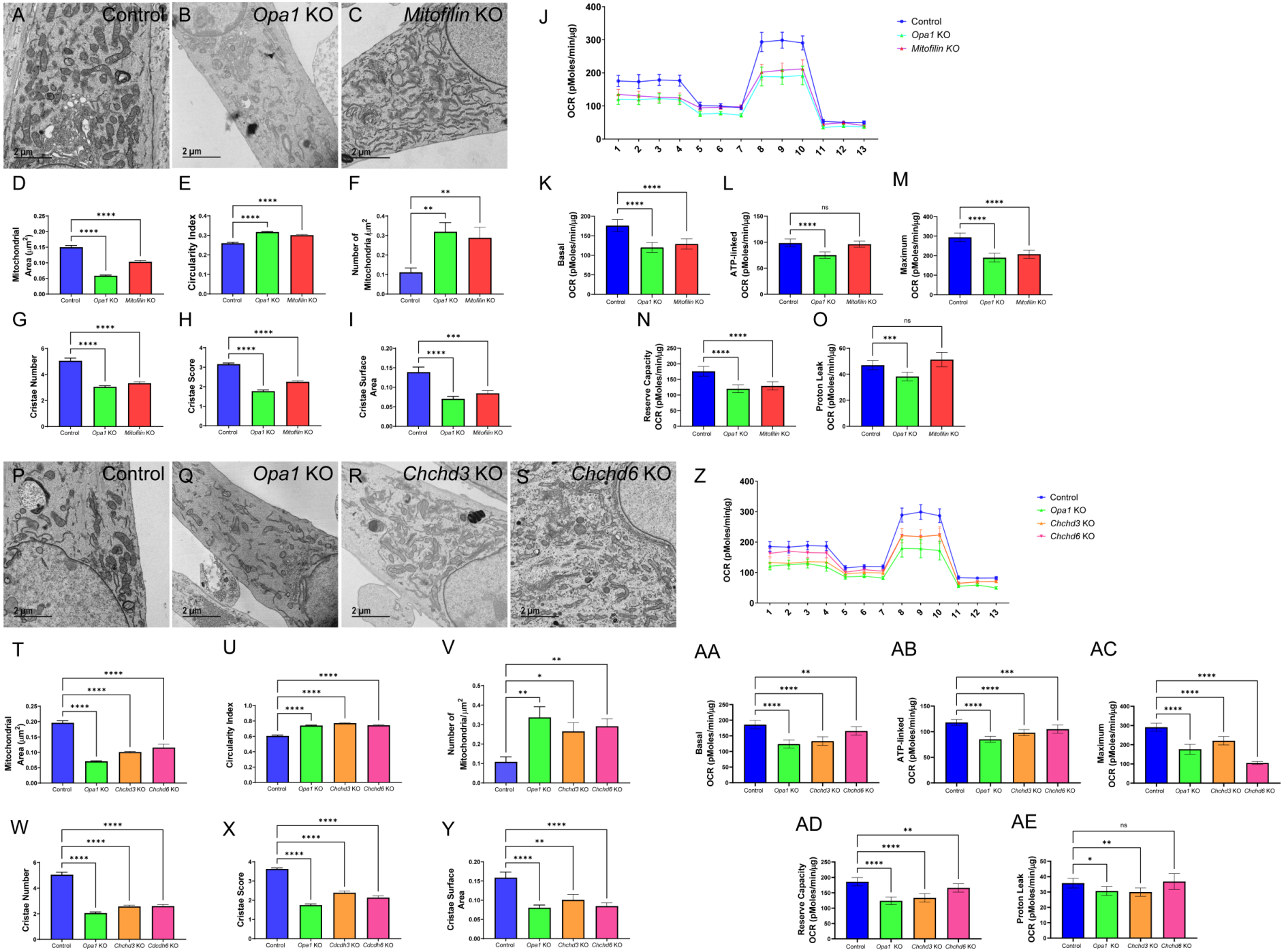
A Control
B Opa1 KO
C Mitofilin KO
2 µm
J
OCR (pMoles/min/µg)
Control
Opa1 KO
Mitofilin KO
D
Mitochondrial Area (µm²)
E
Circularity Index
F
Number of Mitochondria/µm²
K
Basal OCR (pMoles/min/µg)
L
ATP-linked OCR (pMoles/min/µg)
M
Maximum OCR (pMoles/min/µg)
G
Cristae Number
H
Cristae Score
I
Cristae Surface Area
N
Reserve Capacity OCR (pMoles/min/µg)
O
Proton Leak OCR (pMoles/min/µg)
P Control
Q Opa1 KO
R Chchd3 KO
S Chchd6 KO
Z
Control
Opa1 KO
Chchd3 KO
Chchd6 KO
T
U
V
AA
AB
AC
W
X
Y
AD
AE
Cdcdh6 KO

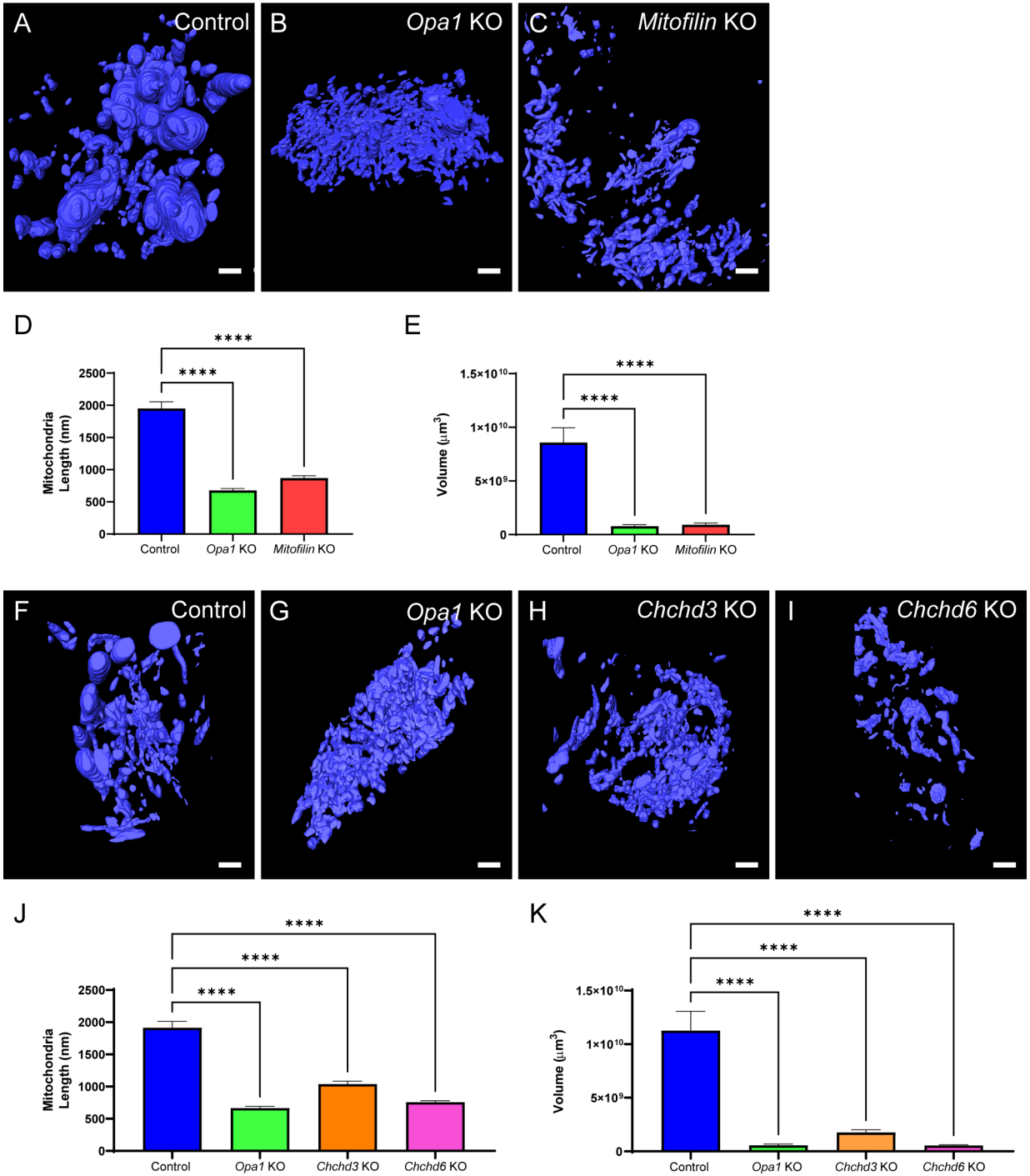
A
Control
B
Opa1 KO
C
Mitofilin KO
D
Mitochondria Length (nm)
2500
2000
1500
1000
500
0
****
****
Control
Opa1 KO
Mitofilin KO
E
Volume (μm³)
1.5×10¹⁰
1×10¹⁰
5×10⁹
0
****
****
Control
Opa1 KO
Mitofilin KO
F
Control
G
Opa1 KO
H
Chchd3 KO
I
Chchd6 KO
J
Mitochondria Length (nm)
2500
2000
1500
1000
500
0
****
****
****
Control
Opa1 KO
Chchd3 KO
Chchd6 KO
K
Volume (μm³)
1.5×10¹⁰
1×10¹⁰
5×10⁹
0
****
****
****
Control
Opa1 KO
Chchd3 KO
Chchd6 KO

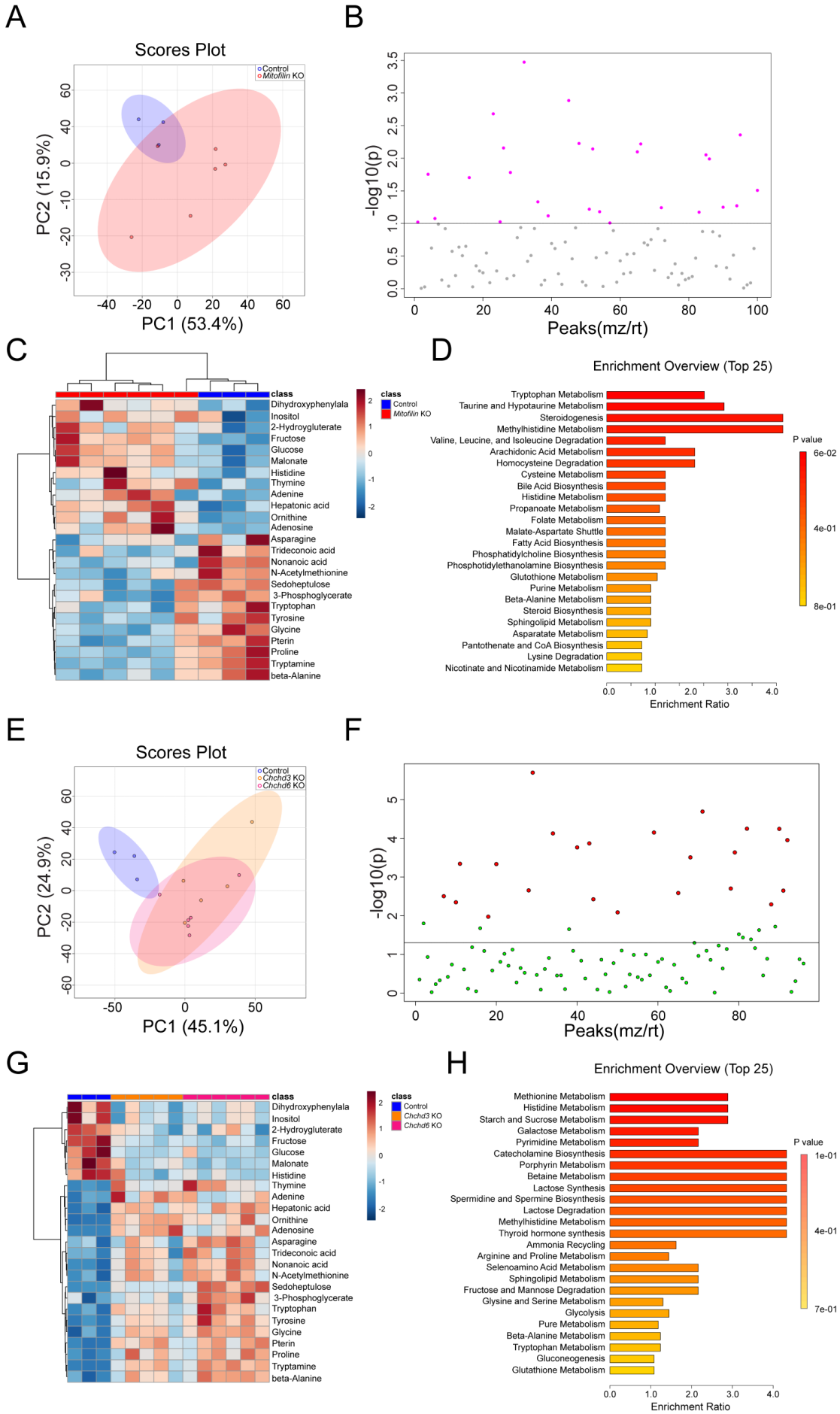
A
Scores Plot
Control
Mitofilin KO
PC2 (15.9%)
PC1 (53.4%)
B
-log10(p)
Peaks(mz/rt)
C
class
Control
Mitofilin KO
Dihydroxyphenylala
Inositol
2-Hydroygluterate
Fructose
Glucose
Malonate
Histidine
Thymine
Adenine
Hepatonic acid
Ornithine
Adenosine
Asparagine
Trideconoic acid
Nonanoic acid
N-Acetylmethionine
Sedoheptulose
3-Phosphoglycerate
Tryptophan
Tyrosine
Glycine
Pterin
Proline
Tryptamine
beta-Alanine
D
Enrichment Overview (Top 25)
Tryptophan Metabolism
Taurine and Hypotaurine Metabolism
Steroidogenesis
Methylhistidine Metabolism
Valine, Leucine, and Isoleucine Degradation
Arachidonic Acid Metabolism
Homocysteine Degradation
Cysteine Metabolism
Bile Acid Biosynthesis
Histidine Metabolism
Propanoate Metabolism
Folate Metabolism
Malate-Aspartate Shuttle
Fatty Acid Biosynthesis
Phosphatidylcholine Biosynthesis
Phosphotidylethanolamine Biosynthesis
Glutothione Metabolism
Purine Metabolism
Beta-Alanine Metabolism
Steroid Biosynthesis
Sphingolipid Metabolism
Asparatate Metabolism
Pantothenate and CoA Biosynthesis
Lysine Degradation
Nicotinate and Nicotinamide Metabolism
P value
6e-02
4e-01
8e-01
Enrichment Ratio
E
Scores Plot
Control
Chchd3 KO
Chchd6 KO
PC2 (24.9%)
PC1 (45.1%)
F
-log10(p)
Peaks(mz/rt)
G
class
Control
Chchd3 KO
Chchd6 KO
Dihydroxyphenylala
Inositol
2-Hydroygluterate
Fructose
Glucose
Malonate
Histidine
Thymine
Adenine
Hepatonic acid
Ornithine
Adenosine
Asparagine
Trideconoic acid
Nonanoic acid
N-Acetylmethionine
Sedoheptulose
3-Phosphoglycerate
Tryptophan
Tyrosine
Glycine
Pterin
Proline
Tryptamine
beta-Alanine
H
Enrichment Overview (Top 25)
Methionine Metabolism
Histidine Metabolism
Starch and Sucrose Metabolism
Galactose Metabolism
Pyrimidine Metabolism
Catecholamine Biosynthesis
Porphyrin Metabolism
Betaine Metabolism
Lactose Synthesis
Spermidine and Spermine Biosynthesis
Lactose Degradation
Methylhistidine Metabolism
Thyroid hormone synthesis
Ammonia Recycling
Arginine and Proline Metabolism
Selenoamino Acid Metabolism
Sphingolipid Metabolism
Fructose and Mannose Degradation
Glysine and Serine Metabolism
Glycolysis
Pure Metabolism
Beta-Alanine Metabolism
Tryptophan Metabolism
Gluconeogenesis
Glutathione Metabolism
P value
1e-01
4e-01
7e-01
Enrichment Ratio